d·Collection

理 學 碩 士 學 位 論 文

Computational and experimental studies on boron based thermally activated delayed fluorescence materials

(붕소 기반 열활성 지연 형광 물질의 계산 및 실험 연구)

蔚 山 大 學 校 大 學 院

化 學 科

李 泰 煥

Computational and experimental studies on boron based thermally activated delayed fluorescence materials

指 導 敎 授 정 재 훈
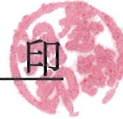
指 導 敎 授 이 민 형

이 論文을 理學碩士 學位 論文으로 제출함

2023年 8月

蔚 山 大 學 校 大 學 院

化 學 科

李 泰 煥

李 泰 煥의 理學碩士 學位 論文을 認准함

審査委員　정 재 훈　　印

審査委員　이 민 형　　印

審査委員　우 상 국　　印

蔚 山 大 學 校 大 學 院

2023年 8月

Contents

0. Abstract.

0.1. Abstract in English

1. Experimental and computational study on Multiple-resonance (MR) TADF including carborane

The unique structure of Multiple-Resonance thermally activated delayed fluorescence (MR-TADF) emitters, with the HOMO and LUMO localized on different atoms, results in short-range charge transfer (SRCT) transitions, leading to narrowband emissions. This implies that the electronic coupling between the carborane and the B,N-doped MR-emitting core will differ from that observed in conventional caroborane luminophores. Furthermore, introducing carborane into either the dominant HOMO or LUMO position may have distinct effects on the excited-state properties. To investigate the impact of carborane on the photophysical and electroluminescent properties of MR-TADF emitters, we present two carborane-appended MR-TADF emitters, 2CB-BuDABNA (1) and 3CB-BuDABNA (2), along with a reference emitter, BuDABNA (3). Our findings demonstrate that the emission characteristics of the MR-emitting core are retained and can be fine-tuned by the carborane substitution, without inducing charge transfer (CT) emission.

2. Computational study on Donor-Acceptor TADF

The photophysical properties of three donor-acceptor-type TADF emitters (PXZBAO (**1**), PXZBTO (**2**), and PXZBPO (**3**)) are herein investigated using time-dependent density functional theory (TDDFT) calculations. Photoluminescence experiments revealed that the emitters exhibit the red (**1**) to orange (**3**) emissions with an increase in the π-expansion in the BCO acceptors. This unusual emission color shift can be explained by the LUMO energy

level of TADF emitter, which is attributed to the strength of local aromaticity for the π-expanded unit of BCO acceptors, for which the squared effective ring electron density (ERED^2) was evaluated as a descriptor for the local aromaticity of a ring over all Kekulé structures based on WFRT analysis. Also, To provide photophysical insights of their TADF processes, we evaluated the spin orbit coupling matrix elements (SOCME) between the S_1 and T_n (n = 1 and 2) excited states. The SOCME between the S_1 and T_2 states is much larger than that between the corresponding S_1 and T_1 states for all compounds, as expected by El-Sayed rule.

0.2. Summary in Korean

1. 카보레인을 포함하는 다중공명 TADF 에 대한 실험 및 전산 연구

HOMO 및 LUMO 가 서로 다른 원자에 국한된 다중 공명 열 활성화 지연 형광(MR-TADF) 방출기의 고유한 구조는 단거리 전하 이동 전이를 일으켜 협대역 방출로 이어집니다. 이는 카보란과 B,N 도핑된 MR 방출 코어 사이의 전자 결합이 기존의 카로보란 발광단에서 관찰되는 것과 다를 것임을 의미합니다. 또한 지배적인 HOMO 또는 LUMO 위치에 카르보란을 도입하면 여기 상태 특성에 뚜렷한 영향을 미칠 수 있습니다. MR-TADF 이미터의 광물리적 및 전자발광 특성에 대한 카르보란의 영향을 조사하기 위해 두 개의 카르보란이 추가된 MR-TADF 이미터인 **2CB-BuDABNA (1)** 및 **3CB-BuDABNA (2)**와 기준 이미터 **BuDABNA (3)**를 제시합니다. 우리의 연구 결과는 MR 방출 코어의 방출 특성이 유지되고 전하 이동 방출을 유도하지 않고 카르보란 치환에 의해 미세 조정될 수 있음을 보여줍니다.

2. 주개-받개 TADF 에 대한 전산 연구

3 개의 도너-억셉터 유형 TADF 방출기(**PXZBAO** (**1**), PXZBTO (**2**) 및 **PXZBPO** (**3**))의 광물리적 특성은 여기에서 TDDFT (시간 종속 밀도 함수 이론) 계산을 사용하여 조사됩니다. 분광실험은 방출기가 BCO 수용체에서 π-팽창이 증가함에 따라 빨간색(**1**)에서 주황색(**3**) 방출을 나타내는 것으로 나타났습니다. 이 비정상적인 방출 색 이동은 TADF 방출체의 LUMO 에너지 준위로 설명할 수 있으며, 이는 BCO 수용체의 π-확장 단위에 대한 국소 방향족성의 강도에 기인하며, 제곱된 유효 고리 전자 밀도(ERED2)는 다음과 같이 평가되었습니다. WFRT 분석을 기반으로 하는 모든 Kekulé 구조에 대한 고리의 국부적 방향성에 대한 설명자입니다. 또한 TADF 프로세스의 광물리학적 통찰력을 제공하기 위해 S_1 과 T_n ($n = 1$ 및 2) 여기 상태 사이의 스핀 궤도 결합 매트릭스 요소 (SOCME)를 평가했습니다. S_1 과 T_2 상태 사이의 SOCME 는 티-Sayed 규칙에서 예상한 대로 모든 화합물에 대한 해당 S_1 과 T_1 상태 사이의 SOCME 보다 훨씬 큽니다.

I. Introduction

1.0. Introduction of thermally activated delayed fluorescence (TADF)

Thermally activated delayed fluorescence (TADF) compounds have received a great deal of attention as efficient emitters in organic light-emitting diodes (OLEDs) since TADF-OLEDs can overcome the issues in phosphorescent OLEDs. [1-8]Much interest and research have been ongoing on TADF molecules in recent years. TADF molecules have the advantage of a theoretical internal quantum efficiency of 100% because they use both singlet and triplet states of electrons (**Figure 1**). The reverse intersystem crossing (RISC) rate constant (k_{risc}) between the singlet and triplet states, occurs more efficiently as the energy gap between the singlet and triplet states, ΔE_{st}, becomes smaller and the spin-orbit coupling (SOC) constant becomes larger.[2,6,8] The ΔE_{st} plays a crucial role in achieving TADF. Conventional TADF materials often adopt twisted donor-acceptor (D-A) structures, where different electron-donating and electron-accepting units are carefully selected to minimize ΔE_{ST}.[1-8] However, increasing the spatial separation between the highest occupied molecular orbital (HOMO) and lowest unoccupied molecular orbital (LUMO) leads to a decrease in the transition oscillator strength (*f*), resulting in reduced photoluminescence (PL) quantum yield (PLQY,Φ_{PL}) and electroluminescence (EL) efficiency of the device. Additionally, the D-A molecular design, involving strong intramolecular charge transfer (ICT), inevitably leads to significant structural relaxation in the excited state (S_1) and substantial vibronic couplings between the S_1 and ground (S_0) states. Consequently, this design tendency produces a broad emission spectrum with a large full width at half maximum (FWHM) of approximately 70–100 nm and a considerable Stokes shift, which negatively affects the emission color purity. Hence, the

development of narrowband emissive TADF materials becomes critical to address the color

purity challenges associated with conventional TADF materials.

.
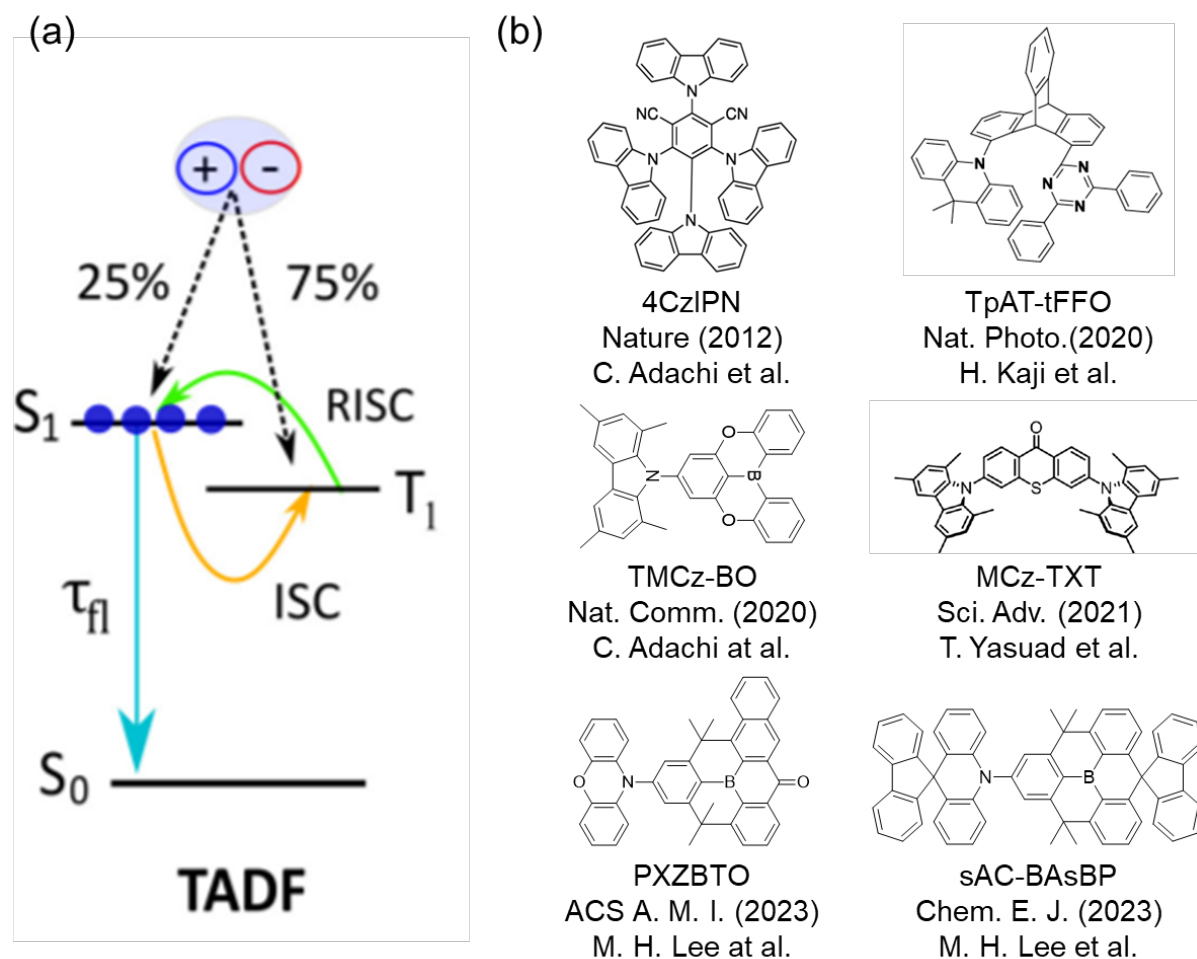
Figure 1. (a) Concept of TADF compounds. (b) Structure of D-A TADF compounds including

boron.

Therefore In 2016, an intriguing design strategy for TADF materials based on the multiple-

resonance (MR) effect was proposed.[16] Leveraging the remarkable potential to overcome the

aforementioned limitations of D-A type TADF materials, organoboron MR-TADF materials

designed with rigid polycyclic aromatic frameworks exhibited exceptionally sharp blue

emission spectra with narrow FWHMPL values as low as 33–34 nm. Simultaneously, these

materials demonstrated impressive OLED performance, achieving maximum external EL quantum efficiency (EQE_{max}) exceeding 20% and high EL color purity (FWHMEL = 28 nm).[16, 104] Due to the alternating localization of the HOMO and LUMO on the different atoms of the rigid and planar MR core, the MR-TADF emitters undergo suppressed vibronic coupling between the ground (S_0) and singlet excited (S_1) states, as well as reduced structural relaxation at the excited states.[16, 104] As a result, these emitters exhibited emissions with narrow FWHM (< 30 nm), small Stokes shifts, and high PLQYs (**Figure 2**).[16, 104]These emission characteristics are particularly beneficial for achieving high efficiency and color purity in deep blue OLEDs. However, MR-TADF-compounds based on mono-boron emitters experienced significant efficiency roll-off due to the presence of long-lived triplet excitons, which were caused by a sluggish RISC process of the emitters (k_{risc}: ~10^3–10^4 s^{-1}). Consequently, extensive research efforts are currently underway to address these limitations and explore diverse photophysical properties.
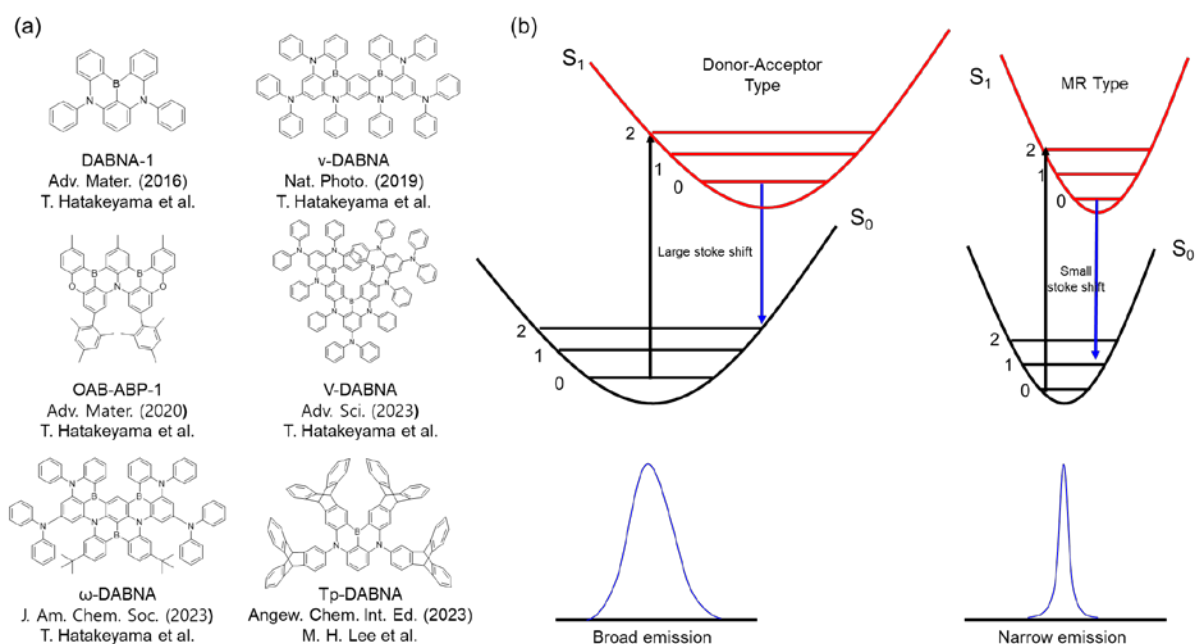
Figure 2. (a) Structure of MR TADF compounds. (b) Schematic picture for the suppression of vibronic coupling between the ground state (S_0) and singlet excited state (S_1).

Unlike MR-TADF molecules, D-A TADF molecules have fast k_{rics} and good OLED efficiency.[9] The K_{risc} in TADF molecules was primarily attributed to the SOC value between the first triplet and the first singlet states. However, this explanation was insufficient in providing a clear mechanism. To overcome this limitation, the El-Sayed rule, which describes the intersystem crossing between excited states, particularly those involving excited states of excited states, was utilized to explain the mechanism. The El-Sayed rule, proposed by Tarek El-Sayed, states that the spin-orbit coupling between the $^1\pi\pi^*$ and $^3\pi\pi^*$ states, as well as the $^1n\pi^*$ and $^3n\pi^*$ states, is forbidden.[13] According to this rule, crossings between the $^1\pi\pi^*$ and $^3\pi\pi^*$ states and between the $^1n\pi^*$ and $^3n\pi^*$ states do not occur, while crossings between the $^1n\pi^*$ and $^3\pi\pi^*$ states and between the $^1\pi\pi^*$ and $^3n\pi^*$ states are allowed. TADF molecules of the D-A type primarily undergo ICT involving the singlet and triplet excited states, predominantly exhibiting $\pi\pi^*$ transitions. However, these phenomena cannot be adequately explained by the El-Sayed rule due to the small SOC values involved. Therefore, based on the El-Sayed rule, it was proposed that transitions occur between higher excited triplet states and the singlet excited states, leading to efficient device materials with TADF properties. Among various TADF molecules, those containing boron have been studied as device materials with external quantum efficiencies of over 30%.[9] Therefore, I conducted experimental and computational research on TADF molecules containing boron as follows.

1.1. General chemistry of carborane

Carboranes are a class of chemical compounds that contain carbon (C), boron (B), and hydrogen (H) atoms. They are characterized by a three-dimensional polyhedral structure formed by a cluster of boron and carbon atoms, with hydrogen atoms attached to the vertices

of the polyhedron.[33] (**Figure 3**) The general formula for carborane is $C_2B_nH_{n+2}$, where n represents the number of boron atoms in the cluster. The most common carborane is ortho-carborane, $C_2B_{10}H_{12}$, which consists of a 12-vertex icosahedral structure formed by two carbon atoms and ten boron atoms.[27-35] Carborane possess unique properties that make them valuable in various applications. Some of their notable characteristics include thermal and chemical stability, high electron deficiency, three-dimensional structure, and solubility. Carborane exhibit excellent thermal stability, allowing them to withstand high temperatures without decomposing or degrading. They are chemically inert and resistant to oxidation, making them suitable for use in harsh chemical environments. The boron atoms in carborane are electron-deficient, making them electron-accepting species. This property enables carborane to participate in electron-transfer reactions and coordinate with Lewis bases. The three-dimensional shape of carborane provides steric protection to the central carbon atoms, enhancing their stability and preventing undesired interactions. Carborane are generally insoluble in polar solvents but exhibit varying solubility in nonpolar and organic solvents.[105]
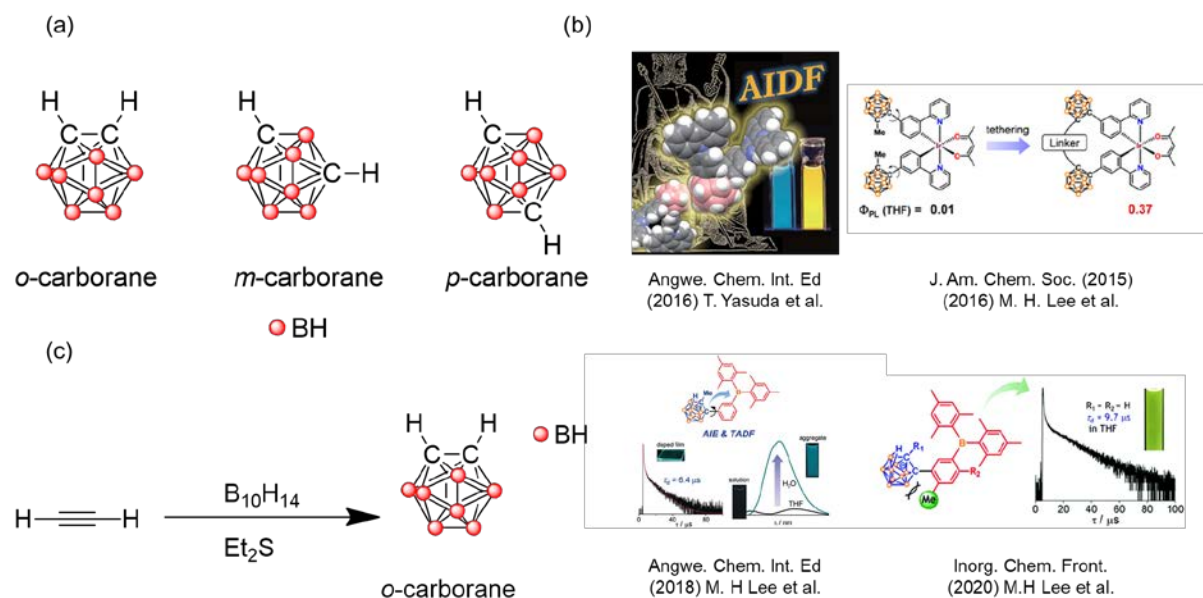
Figure 3 (a) Structure of carbonran. (b) carborane as Luminophores. (c) The scheme of the *o*-carborane

Their unique electronic properties make carborane useful in the development of electronic devices, such as diodes, transistors, and sensors. In summary, carborane are a class of compounds with a unique polyhedral structure composed of carbon, boron, and hydrogen atoms. Their remarkable stability, chemical inertness, and electron-accepting properties make them valuable in various fields, ranging from electronics to medicine and catalysis.[105]

1.2. Experimental and computational study on Multiple-Resonance (MR) TADF including *o*-carborane

The unique structure of MR-TADF emitters, with the HOMO and LUMO localized on different atoms, results in short-range charge transfer (SRCT) transitions, leading to narrowband emissions. This implies that the electronic coupling between the *o*-carborane and the B,N-doped MR-emitting core will differ from that observed in conventional *o*-carboranyl luminophores. Furthermore, introducing *o*-carborane into either the dominant HOMO or LUMO position may have distinct effects on the excited-state properties. To investigate the impact of *o*-carborane on the photophysical and electroluminescent properties of MR-TADF emitters, we present two *o*-carborane-appended MR-TADF emitters, **2CB-BuDABNA** (**1**) and **3CB-BuDABNA** (**2**), along with a reference emitter, **BuDABNA** (**3**). Our findings demonstrate that the emission characteristics of the MR-emitting core are retained and can be fine-tuned by the *o*-carborane substitution, without inducing charge transfer (CT) emission. Further details will be discussed in Chapter 3.1.

1.3. Computational study on Donor-Acceptor TADF

The photophysical properties of three donor-acceptor-type TADF emitters (PXZBAO (**1**), PXZBTO (**2**), and PXZBPO (**3**)) are herein investigated using time-dependent density functional theory (TDDFT) calculations. Photoluminescence experiments revealed that the emitters exhibit the red (**1**) to orange (**3**) emissions with an increase in the π-expansion in the BCO acceptors.[11] This unusual emission color shift can be explained by the LUMO energy level of TADF emitter, which is attributed to the strength of local aromaticity for the π-expanded unit of BCO acceptors, for which the squared effective ring electron density (ERED^2) was evaluated as a descriptor for the local aromaticity of a ring over all Kekulé structures based on WFRT analysis.[12] Also, To provide photophysical insights of their TADF processes, we evaluated the SOC matrix elements (SOCME) between the S_1 and T_n ($n = 1$ and 2) excited states. The SOCME between the S_1 and T_2 states is much larger than that between the corresponding S_1 and T_1 states for all compounds, as expected by El-Sayed rule.[13] Details will be explained in chapter 3.2

2. Methodological background

2.1. Density functional theory

The density functional theory (DFT) has emerged as a crucial tool in various scientific disciplines. In this thesis, we employ a computational approach rooted in DFT to investigate surface phenomena like adsorption and chemical reactions. Our work collaborates closely with experimental research, utilizing scanning tunneling microscopy. This chapter aims to provide a concise overview of the essential aspects of electronic structure theory, beginning with the Schrödinger equation for many-body systems and culminating in the Kohn-Sham density functional equation.[14-16] The mathematical notations used in this chapter draw heavily from Richard M. Martin's book, "Electronic Structure: Basic Theory and Practical Methods.[14]" Lastly, we include a brief introduction to scanning tunneling microscopy in the concluding section.

2.1.1. Hohenberg-Kohn theorems

According to the fundamental philosophy of DFT, the properties of a system consisting of numerous interacting particles can be determined by a functional that depends on the electron density $n_0(r)$ of the ground state. This principle is rooted in the theorems established by P. Hohenberg and W. Kohn in 1964, which govern the behavior of such functionals.[20]

- **Theorem I**: For any system of interacting particles in an external potential $V_{ext}(r)$, the potential $V_{ext}(r)$ is determined uniquely, except for a constant, by the ground state particle density $n_0(r)$.

Therefore, if the Hamiltonian is uniquely determined by the ground state density $n_0(r)$ according to the Hohenberg-Kohn theorem I, the wavefunction of any state can be determined

by solving the Schrödinger equation with this Hamiltonian. Thus, all properties of the system are completely determined by ground state density.

- **Theorem II**: A universal functional for the energy $E[n]$ in terms of the density $n(r)$ can be defined, as valid for any external potential $V_{ext}(r)$. For any particular $V_{ext}(r)$, the exact ground state energy of the system is the global minimum value of this function, and the density $n(r)$ that minimizes the functions the exact ground state density $n_0(r)$.

Therefore, if the function including all internal energies (kinetic and potential energies) of the interacting electron system is known, the exact ground state density of energy by minimizing the total energy of the system using the variation principle with respect to the density function $n(r)$. However, the Hohenberg-Kohn theorem II does not provide any guidance concerning the excited states of the electrons.

2.1.2. The Kohn-Sham approach

The Kohn-Sham approach is to replace the difficult interacting many-body system with a different auxiliary system which can be more easily solved. The *ansatz* of Kohn and Sham assumes that the ground state density of the original interacting system is equal to that of some chosen non-interacting system.[18,19] This leads to independent-particle equations for the non-interacting system that can be considered exactly soluble with all the difficult many-body terms incorporated into an exchange-correlation function of the density. Therefore, the accuracy of Kohn-Sham's approach is only limited by the exchange-correlation functional.

The Kohn-Sham construction of an auxiliary system rests upon two assumptions: (1) the exact ground state density can be represented by the ground state density of an auxiliary system of non-interacting particles. This leads to the relation of the actual and auxiliary systems. (2) The

auxiliary Hamiltonian is chosen to have the usual kinetic operator and an effective local potential $V_{\text{eff}}^{\sigma}(\mathbf{r})$ acting on an electron of spin σ at point $\mathbf{r}$.

The auxiliary Hamiltonian for the independent-particle system is

$$\hat{H}_{\text{aux}}^{\sigma} = -\frac{1}{2}\nabla^2 + V^{\sigma}(\mathbf{r}) \tag{1.00}$$

.

The density of the auxiliary system is given by sums of squares of the orbitals for each spin

$$n(\mathbf{r}) = \sum_{\sigma} n(\mathbf{r},\sigma) = \sum_{\sigma}\sum_{i=1}^{N^{\sigma}}\left|\psi_i^{\sigma}(\mathbf{r})\right|^2 \tag{1.10}$$

,

the independent-particle kinetic energy T_s is given by

$$T_s = -\frac{1}{2}\sum_{\sigma}\sum_{i=1}^{N^{\sigma}}\left\langle\psi_i^{\sigma}\left|\nabla^2\right|\psi_i^{\sigma}\right\rangle = \frac{1}{2}\sum_{\sigma}\sum_{i=1}^{N^{\sigma}}\int d^3r\left|\nabla\psi_i^{\sigma}(\mathbf{r})\right|^2 \tag{1.11}$$

,

and we define the classical Coulomb interaction energy of the electron density $n(\mathbf{r})$ interacting with itself, i.e., the Hartree energy.

$$E_{\text{Hartree}}[n] = \frac{1}{2}\int d^3r d^3r' \frac{n(\mathbf{r})n(\mathbf{r}')}{\left|\mathbf{r}-\mathbf{r}'\right|} \tag{1.12}$$

.

The [n] denotes a functional of the density $n(\mathbf{r},\sigma)$ which depends on both position in space $\mathbf{r}$ and spin σ. Now, the Kohn-Sham approach to the full interacting many-body problem is to rewrite the Hohenberg-Kohn expression for the ground state energy functional in the form

$$E_{\text{KS}} = T_s[n] + \int d\mathbf{r} V_{\text{ext}}(\mathbf{r})n(\mathbf{r}) + E_{\text{Hartree}}[n] + E_{II} + E_{\text{xc}}[n] \tag{1.13}$$

.

Here, all many-body effects of exchange of correlation are grouped into the exchange-correlation energy E_{xc}.

$$E_{xc}[n] = \langle \hat{T} \rangle - T_s[n] + \langle \hat{V}_{int} \rangle - E_{Hartree}[n] \ .$$ (1.14)

If the universal functional $E_{xc}[n]$ defined in (1.14) were known, then the exact ground state energy and density of the many-body electron problem could be found by self-consistently solving the Kohn-Sham equations for independent particles.

The Kohn-Sham auxiliary system for the ground state can be viewed as a problem of minimization with respect to density $n(\mathbf{r},\sigma)$. Because T_s is the functional of the orbitals and all other terms are functionals of the density, one can vary the wavefunctions and use the chain rule to derive the variational equation

$$\frac{\delta E_{KS}}{\delta \psi_i^{\sigma*}(\mathbf{r})} = \frac{\delta T_s}{\delta \psi_i^{\sigma*}(\mathbf{r})} + \left[\frac{\delta E_{ext}}{\delta n(\mathbf{r},\sigma)} + \frac{\delta E_{Hartree}}{\delta n(\mathbf{r},\sigma)} + \frac{\delta E_{xc}}{\delta n(\mathbf{r},\sigma)} \right] \frac{\delta n(\mathbf{r},\sigma)}{\delta \psi_i^{\sigma*}(\mathbf{r})} = 0 \ ,$$ (1.15)

subject to the orthonormalization constraints

$$\langle \psi_i^{\sigma} | \psi_j^{\sigma'} \rangle = \delta_{i,j}\delta_{\sigma,\sigma'} \ .$$ (1.16)

Using expressions (1.11) and (1.12) for $n^{\sigma}(\mathbf{r})$ and T_s, which give

$$\frac{\delta T_s}{\delta \psi_i^{\sigma*}(\mathbf{r})} = -\frac{1}{2}\nabla^2 \psi_i^{\sigma}(\mathbf{r}) \ ; \quad \frac{\delta n(\mathbf{r},\sigma)}{\delta \psi_i^{\sigma*}(\mathbf{r})} = \psi_i^{\sigma}(\mathbf{r}) \ ,$$ (1.17)

and using the Lagrange multiplier method leads to Kohn-Sham Schrödinger-like equations:

$$\left(H_{KS}^{\sigma} - \varepsilon_i^{\sigma} \right)\psi_i^{\sigma}(\mathbf{r}) = 0 \ ,$$ (1.18)

where ε_i are the eigenvalues, and H_{KS} is the effective Hamiltonian

$$H_{KS}^{\sigma} = -\frac{1}{2}\nabla^2 + V_{KS}^{\sigma}(\mathbf{r}) \ ,$$ (1.19)

with,

$$V_{\text{KS}}^{\sigma}(\mathbf{r}) = V_{\text{ext}}(\mathbf{r}) + \frac{\delta E_{\text{Hartree}}}{\delta n(\mathbf{r},\sigma)} + \frac{\delta E_{\text{xc}}}{\delta n(\mathbf{r},\sigma)} = V_{\text{ext}}(\mathbf{r}) + V_{\text{Hartree}}(\mathbf{r}) + V_{\text{xc}}^{\sigma}(\mathbf{r}) \qquad (1.20)$$

Kohn-Sham equations have the form of independent particle equations with a potential that must be solved self-consistently with the resulting energy or Hellmann-Feynman force. (The typical iterative process is shown in **Figure 4**.) These equations would lead to the exact ground state density and energy for the interaction system, if the exact functional $E_{\text{xc}}[n]$ were known. Therefore, the major problem in DFT is deriving suitable formulas for the exchange-correlation term.
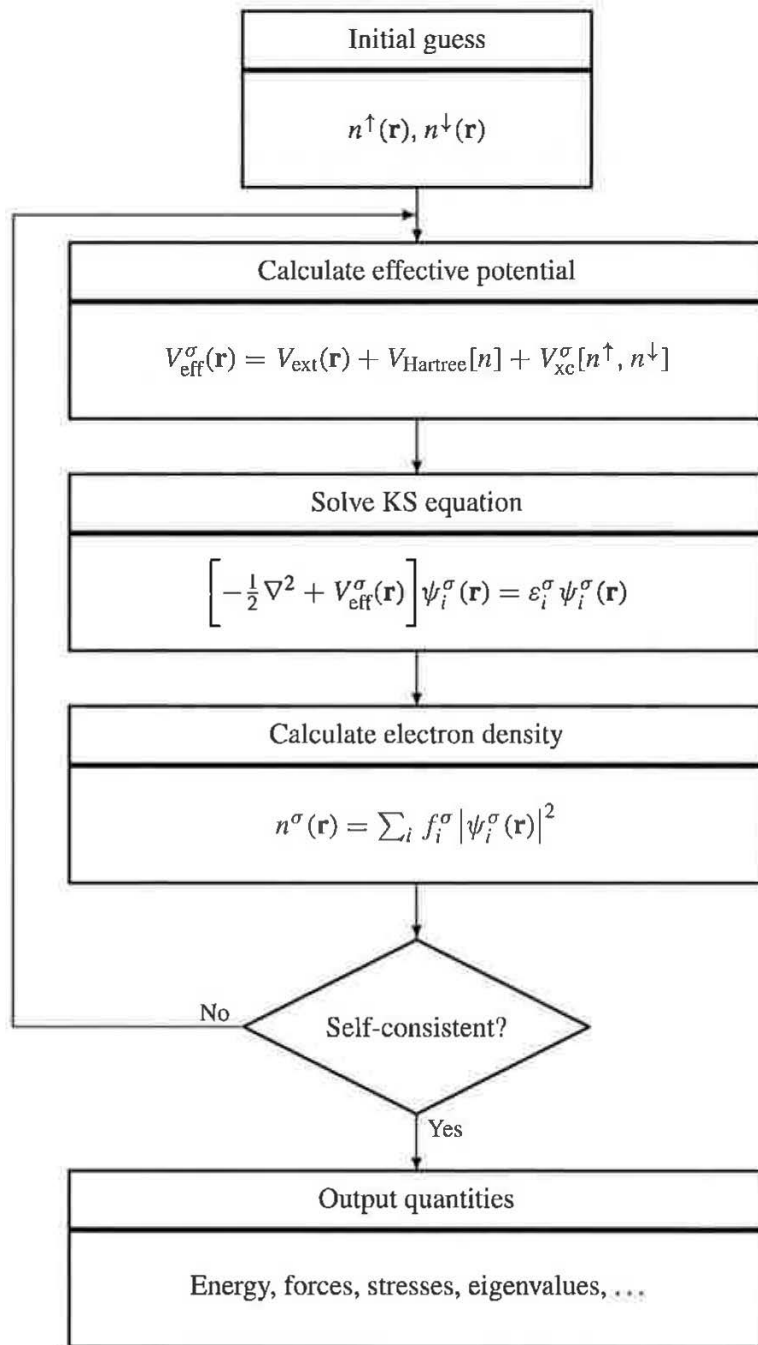
Figure 4. Schematic representation of the self-consistent loop for solution of Kohn-Sham equations. [Adapted from Reference 20]

2.1.3. The exchange-correlation functional

In the practical use of DFT, the most general approximations to describe $E_{xc}[n]$ are local density approximation (LDA) (or more generally, the local spin density approximation (LSDA)) and generalized gradient approximation (GGA).

Usually solids can be considered as close to the limit of the homogeneous electron gas. In that limit, the effects of exchange and correlation are local in character. Therefore, in the case of LDA, the exchange-correlation energy is simply an integral over all space with the exchange-correlation energy density at each point assumed to be the same as in a homogenous electron gas with that density,

$$
\begin{aligned}
E_{xc}^{LSDA}[n^\uparrow, n^\downarrow] &= \int d^3 r n(\mathbf{r}) \varepsilon_{xc}^{hom}(n^\uparrow(\mathbf{r}), n^\downarrow(\mathbf{r})) \\
&= \int d^3 r n(\mathbf{r})[\varepsilon_x^{hom}(n^\uparrow(\mathbf{r}), n^\downarrow(\mathbf{r})) + \varepsilon_c^{hom}(n^\uparrow(\mathbf{r}), n^\downarrow(\mathbf{r}))].
\end{aligned}
\tag{1.21}
$$

For unpolarized systems, the LDA is found simply by setting $n^\uparrow(\mathbf{r}) = n^\downarrow(\mathbf{r}) = n(\mathbf{r})/2$. LDA is best for solids close to a homogeneous gas and worst for very inhomogeneous cases like atoms where the density must go continuously to zero outside the atom. The other approximation is GGA, which is a marked improvement over LDA for many cases. E_{xc} of GGA with a magnitude of the gradient of density $|\nabla n^\sigma|$ is written as

$$
\begin{aligned}
E_{xc}^{GGA}[n^\uparrow, n^\downarrow] &= \int d^3 r n(\mathbf{r}) \varepsilon_{xc}(n^\uparrow, n^\downarrow, |\nabla n^\uparrow|, |\nabla n^\downarrow|, \ldots) \\
&= \int d^3 r n(\mathbf{r}) \varepsilon_x^{hom}(n) F_{xc}(n^\uparrow, n^\downarrow, |\nabla n^\uparrow|, |\nabla n^\downarrow|, \ldots),
\end{aligned}
\tag{1.22}
$$

where F_{xc} is dimensionless and $\varepsilon_x^{hom}(n)$ is the exchange energy of the unpolarized gas. Unlike LDA, the spin-scaling relationship should be considered in GGA, and in particular, for $F_x(n, |\nabla n|)$ of the polarized system. As there are numerous forms that F_x may take, many kinds

of GGA methods have been proposed so far, such as Becke (B88),[21] Perdew and Wang (PW91),[22,23] and Perdew, Becke, and Enzerhof (PBE).[24]

2.1.4. Time-Dependent Density functional theory (TDDFT)

TDDFT represents an extension of ground-state DFT utilized for calculating the electronic structure of molecules and materials in their lowest energy state. In TDDFT, the analysis of electronic excitations considers the electronic density as a function of both space and time. By solving the time-dependent Schrödinger equation within the framework of DFT, the electronic excited states and their corresponding transition energies are obtained. Regarding the time-dependent Kohn-Sham system, the Runge-Gross theorem establishes that the density is uniquely determined by the external potential for a given interaction potential.[25] The Kohn-Sham approach selects a non-interacting system, where the interaction potential is zero, to construct a density equivalent to that of the interacting system. This choice offers advantages in terms of solving non-interacting systems easily, as the wave function of a non-interacting system can be represented as a Slater determinant of single-particle orbitals. These orbitals are determined by single partial differential equations in three variables. Additionally, the kinetic energy of a non-interacting system can be precisely expressed in terms of these orbitals. Consequently, the objective is to determine a potential, denoted as v_s(r,t) or v_{ks} (r,t), that defines a non-interacting Hamiltonian, H_s

$$\hat{H}_{s(t)} = \hat{T} + \hat{V}_{s(t)},$$

(1.22)

which in turn determines a determinantal wave function

$$\hat{H}s(t)\left|\varPhi(t)\right\rangle = i\frac{\partial}{\partial t}\left|\varPhi(t)\right\rangle, \quad \left|\varPhi(0)\right\rangle = \left|\varPhi\right\rangle$$

(1.23)

which is constructed in terms of a set of N orbitals that obey the equation,

2 0

$$\left(-\frac{1}{2}\nabla^2 + vs_{(r,t)}\right)\emptyset_j(r,t) = i\frac{\partial}{\partial t}\emptyset_j(r,t) \quad \emptyset_j(r,0) = \emptyset_j(r) \quad (1.22)$$

and generate a time-dependent density

$$\rho_{S(r,t)} = \sum_{j=1}^{N_h} f_i(t)|\phi_j(r,t)|^2 \quad (1.23)$$

such that ρ_s is equal to the density of the interacting system at all times:

$$\rho_{S(r,t)} = \rho_{S(r,t)} \quad (1.24)$$

It is important to note that in the density expression mentioned above, the summation encompasses all Kohn-Sham orbitals $f_i(t)$, representing the time-dependent occupation number for each orbital. If the potential $v_s(r,t)$ can be determined, or at least approximated well, the original Schrödinger equation, which is a single partial differential equation in 3N variables, is replaced by N differential equations in 3 dimensions. These equations differ only in the initial condition. The challenge lies in determining approximations to the Kohn-Sham potential. Similar to DFT, the time-dependent Kohn-Sham potential is decomposed to extract the external potential of the system and the time-dependent Coulomb interaction, v_J. The remaining component is the exchange-correlation potential:

$$v_s(\mathbf{r},t) = v_{ext}(\mathbf{r},t) + v_J(\mathbf{r},t) + v_{xc}(\mathbf{r},t). \quad (1.25)$$

2.2 Theoretical part

2.2.1. El-Sayed rule

The El-Sayed rule is a rule in photochemistry that describes the relationship between the nature of the electronic transition and the spin state of the excited state. It was proposed by Mostafa El-Sayed in 1963.[13] The El-Sayed rule states that in a photochemical reaction involving a molecule with a ground-state singlet configuration, the probability of the excited state being a singlet state is higher if the electronic transition involves a change in spin multiplicity (i.e., a spin-forbidden transition) than if it involves no change in spin multiplicity (i.e., a spin-allowed transition) (**Figure 5**). Conversely, the probability of the excited state being a triplet state is higher if the electronic transition involves no change in spin multiplicity than if it involves a change in spin multiplicity. The El-Sayed rule is based on the selection rules for electronic transitions, which determine which transitions are allowed or forbidden based on their symmetry properties. The rule has been used to explain the spin-selective behavior of various photochemical reactions, such as triplet-triplet energy transfer and triplet sensitization in organic photovoltaics.
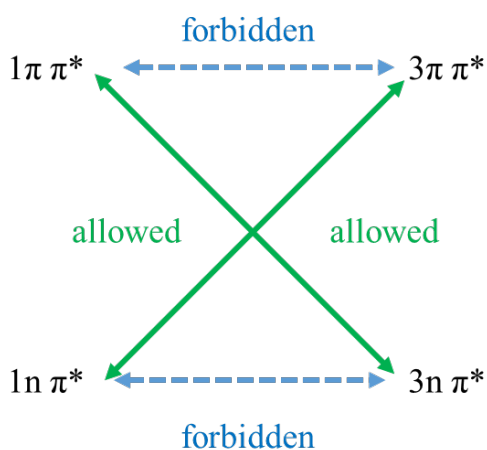

Figure 5. El-Sayed's rule for spin-orbit coupling

2.2.2. Rate constant of non-radiative decay process

 Non-radiative decay rate

The thermal average rate constant from the initial electronic state i, characterized by the vibrational quantum numbers v, to the final electronic state f, characterized by the vibrational quantum numbers u, can be determined using the time-dependent second-order perturbation theory and the Born-Oppenheimer adiabatic approximation. This can be expressed as follows[26].

$$k_{f \leftarrow i} = \frac{2\pi}{\hbar} \sum_{v,u} P_{iv} \left| H'_{fu,\,iv} \right|^2 \times \delta(E_{iv} - E_{fu}) \tag{1.26}$$

 Here, P_{iv} is the Boltzmann distribution function for the initial vibronic manifold; H' denotes the interaction between two different Born−Oppenheimer states; and the delta function δ is to keep the conservation of energy, and it can be expressed as:

$$\hat{H}\psi_{iv} = \hat{H}^{BO}\phi_i(r,Q)\theta_{iv}(Q) + \hat{H}^{SO}\phi_i(r,Q)\theta_{iv}(Q) \tag{1.27}$$

Here $\hat{H}^{BO}$ and $\hat{H}^{SO}$ represent non-adiabatic coupling and SOC. $\emptyset$ and θ are the electron wave function and the nuclear vibration wave function. When transitioning between states with identical spin multiplicities, we can disregard this portion, resulting in the expression of the non-radiative decay rate as follows:

$$k_{f \leftarrow i} = \frac{2\pi}{\hbar^2} \sum_{kl} R_{kl} Z_i^{-1} \sum_{vu} e^{-\beta E_{iv}} \langle \theta_{fu} | \hat{P}_{fk} | \theta_{iv} \rangle \langle \theta_{iv} | \hat{P}_{fl} | \theta_{fu} \rangle \tag{1.28}$$
$$\times \delta(Eiv - Efu)$$

The $R_{kl} = \dfrac{\langle \theta_{fu} | \hat{P}_{fk} | \theta_{iv} \rangle \langle \theta_{iv} | \hat{P}_{fl} | \theta_{fu} \rangle}{}$ and Z_i are the non-adiabatic electronic coupling and the partition function.[26]

3. Results and Discussion

3.1 Experimental study on Multiple-Resonance TADF with carborane

3.1.1 Introduction

Ortho-carborane (1,2-closo-$C_2B_{10}H_{12}$) is an icosahedral boron cluster with electron deficiency, characterized by steric bulkiness and three-dimensional electron delocalization through three-center, two-electron bonds.[27-35] These unique properties have made *o*-carborane a highly attractive steric and electronic building block for constructing various luminophores over the past decade.[35-44] The luminescent characteristics of *o*-carborane-based luminophores are significantly influenced by the inductive electron-withdrawing and conjugation effects of *o*-carborane through 2-R-substitution.[39, 45-51] When *o*-carborane is incorporated into π-conjugated systems, the lowest-energy excited state of the luminophores can be accessed through LE and ICT states, depending on the extent of cage rotation (**Figure 6**, left).[53, 39, 45, 51]

In cases where the $C_{CB}-C_{CB}$ bond is coplanar with the π-systems (angle = 0°), the LE state predominates. Conversely, a perpendicular orientation (angle = 90°) favors the ICT state due to the favorable σ* ($C_{CB}-C_{CB}$) −π* conjugation, which gives rise to LUMO. However, owing to the highly polarizable nature of *o*-carborane, the carboranyl C−C bonds are significantly influenced by the polarity of the medium and the rotational motion of *o*-carborane.[44, 56-63] This variation in the $C_{CB}-C_{CB}$ bond typically leads to emission quenching of *o*-carborane-based luminophores in polar media.[42, 55, 64-67] Conversely, in the solid state, they exhibit intriguing aggregation-induced emission (AIE) due to the restricted rotation of *o*-carborane.[38-39, 48, 68-72] The ICT state in *o*-carborane-based luminophores originates from the π to σ*−π*

transition. Since the π* orbital of an aromatic luminophore is delocalized over the ring system, the electronic conjugation between the carboranyl σ* orbital and the π* orbital significantly influences the LUMO of the luminophores, thereby altering their excited-state properties. Consequently, *o*-carborane-based luminophores, particularly those with a 2-R-substituent on the cage, exhibit broad ICT emissions in the low-energy region, unlike the well-defined, higher-energy LE bands of the parent π-luminophores.
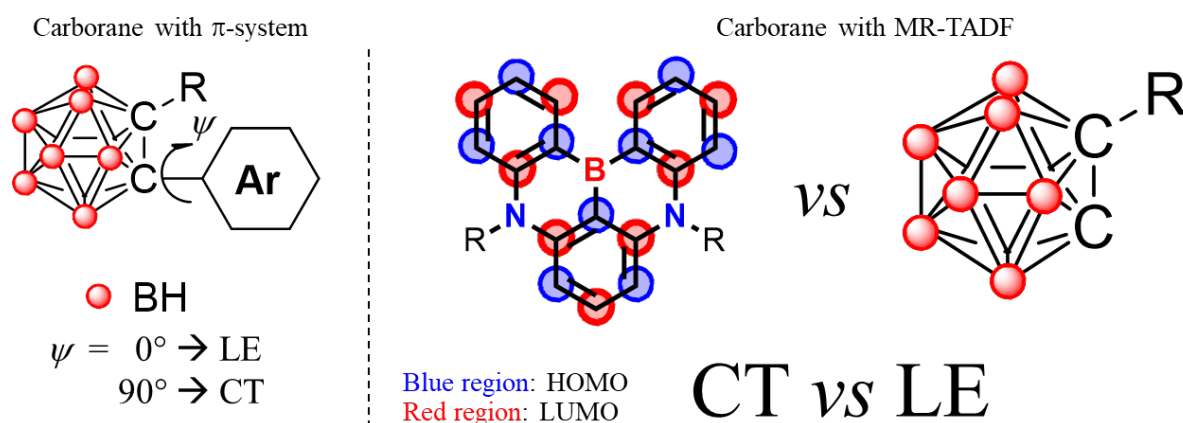

Figure 6. Structures of *o*-carboranyl fluorophores (left) and competitive CT and LE between MR-TADF and *o*-carborane

Considering the development of novel *o*-carboranyl luminophores for optoelectronic materials applications, such as solid-state emitting and stimuli-responsive materials,[36-37, 46, 71, 73] it remains challenging to understand the role of *o*-carborane in controlling the photophysical properties of various luminophores. The choice of the parent π-luminophore becomes a critical factor in tuning the excited-state properties, as the electronic effects of *o*-carborane can vary depending on the employed π-systems. In light of this, we chose to utilize a MR-TADF core as a new luminophoric π-skeleton to create innovative *o*-carboranyl TADF emitters (**Scheme 1**).

MR-TADF emitters, characterized by the localization of HOMO and LUMO on different atoms leading to SRCT transitions, are known for their narrowband emissions.[16, 104] Therefore, it is reasonable to expect that the electronic coupling between the o-carborane and the B,N-doped MR-emitting core will differ from that observed in conventional o-carboranyl luminophores. Furthermore, introducing an o-carborane into either the HOMO or LUMO dominating position may also have a distinct impact on the excited-state properties.

To investigate the effects of o-carborane on the photophysical and electroluminescent properties of MR-TADF emitters, we present two o-carborane-appended MR-TADF emitters, namely **2CB-BuDABNA** (**1**) and **3CB-BuDABNA** (**2**), along with a reference emitter, **BuDABNA** (**3**). Our findings indicate that the emission characteristics of the MR-emitting core are preserved but modulated by the o-carborane substitution, without the occurrence of ICT emission.

3. 1.2 Method

All operations were performed under an inert nitrogen atmosphere using standard Schlenk and glove box techniques. Anhydrous grade solvents (Aldrich) were dried over activated molecular sieves (5Å). Spectrophotometric-grade toluene and tetrahydrofuran were used as received from Aldrich and Alfa, respectively. Commercial reagents were used without further purification after purchase.1-(4-Bromophenyl)-2-methyl-1,2-closo-carborane (1a)[74] and 1-(3-bromophenyl)-2-methly-1.2-closo-carborane (2a)[74] were synthesized according to the reported procedures. Deuterated solvents from Eurisotop were used. NMR spectra were recorded on a Bruker AVANCE III HD 400 (400.13 MHz for ^{1}H, 100.61 MHz for ^{13}C, 128.38 MHz for ^{11}B) spectrometer at ambient temperature. Chemical shifts are given in ppm, and are referenced against external Me$_4$Si (^{1}H, ^{13}C) and BF$_3$·OEt$_2$ (^{11}B). Mass spectra were obtained using a JEOL

JMS700 high-resolution EI-mass spectrometer (HR EI-MS) at the Korea Basic Science Institute, Daegu, Korea. Elemental analyses were performed on a Flash 2000 elemental analyzer (Thermo Scientific). Thermogravimetric analysis (TGA) was performed with a TA Instruments Q50 under an N_2 atmosphere at a heating rate of 10 °C/min. Cyclic voltammetry experiments were carried out using a CHI600E system

The computational study based on TDDFT was performed to investigate not only the geometric and electronic structures of ground and excited states of three compounds (1, 2, and 3) but also their transition properties for excited states. The TDDFT calculations were carried out with Tamm-Dancoff approximation (TDA)[75]. Their ground (S_0) states of compounds were optimized using DFT calculations, and their lowest singlet (S_1) and two triplet (T_1 and T_2) excited states were optimized using TDDFT calculations with the PBE0 hybrid functional[76] and def-2SVP basis set implemented in GAUSSIAN 16 software package.[77] The influence of a different solvent medium (toluene, tetrahydrofuran and gas, respectively) on the geometric and electronic structures was examined using PCM model within self-consistent reaction field (SCRF) approximation.[78]

3. 1.3 *o*-carborane decorated MR TADF Emitters

2CB-BuDABNA (**1**) and 3CB-BuDABNA (**2**) were prepared from the reactions outlined in Scheme 1. Buchwald–Hartwig amination reactions of 4- and 3-bromophenyl substituted methyl-*o*-carboranes (1a and 2a, respectively) with 2-chloro-1,3-diamine led to the *o*-carborane substituted ligands 1b and 2b, respectively. One pot borylation of 1b and 2b by consecutive lithium–chloride exchange, trapping with BBr_3, and electrophilic arene borylation produced the final B,N-doped MR-TADF emitters, **1** and **2**. For comparison, reference emitter,

BuDABNA (**3**) lacking carborane moieties was analogously prepared. Full experimental details are given below.
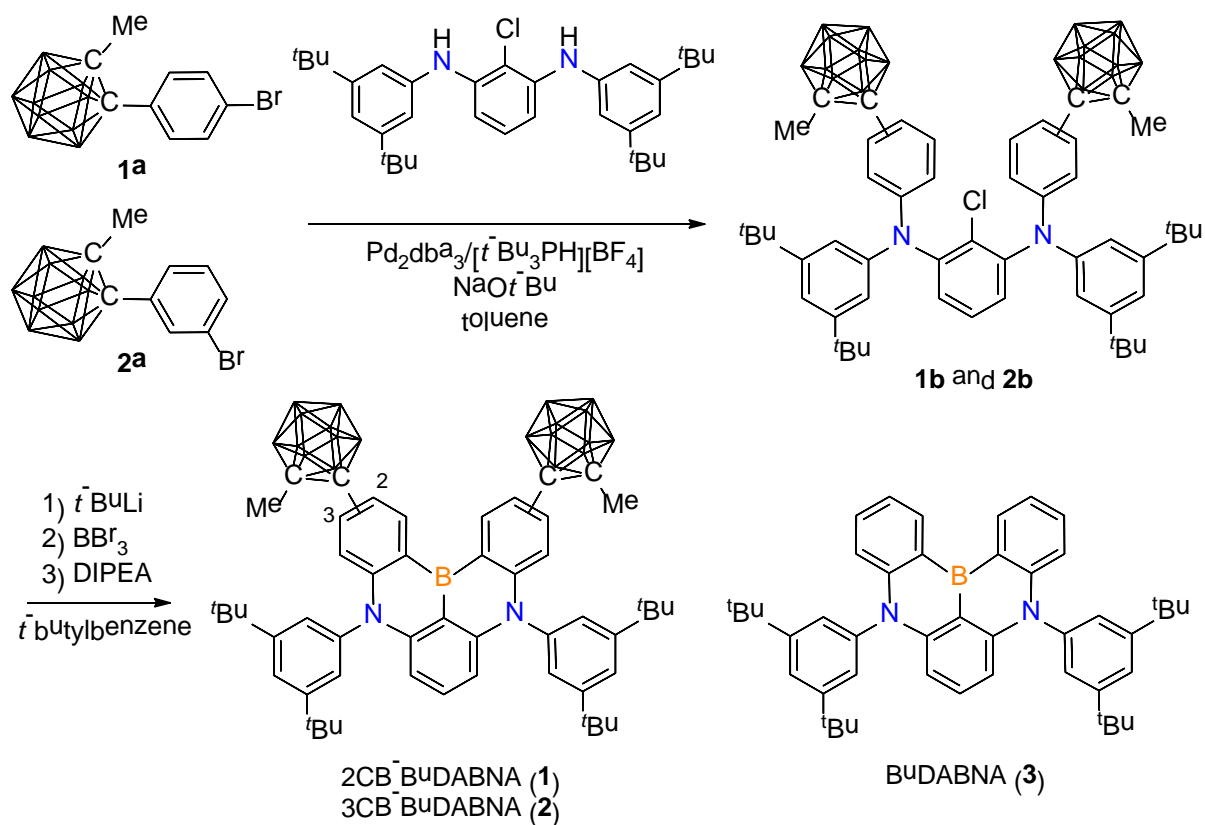
Scheme 1. Synthesis of 2CB-BuDABNA (1) and 3CB-BuDABNA (2)

Synthesis of 1b

A mixture of **1a** (0.67 g, 2.12 mmol), N^1,N^3-bis[3,5-bis(1,1-dimethylethyl)phenyl]-2-chloro-benzene-1,3-diamine (0.50 g, 0.96 mmol), $Pd_2(dba)_3$ (26 mg, 0.03 mmol), $^tBu_3PHBF_4$ (17 mg, 0.06 mmol), and NaOtBu (0.28 g, 2.89 mmol) in dry toluene (20 mL) were stirred overnight at 90 °C. After cooling down to room temperature, the mixture was filtered through a Celite pad, washed with dichloromethane and the filtrate was concentrated under reduced pressure. The crude product was purified by column chromatography on silica gel using dichloromethane/n-hexane (1:10, v/v) as eluent to give 1b as a white solid (Yield: 0.65 g, 69%). ^1H NMR (CDCl$_3$):

δ 7.41–7.32 (m, 5H), 7.28 (s, 2H), 7.19 (t, J = 1.6 Hz, 2H), 6.98 (t, J = 10.5 Hz, 4H), 6.69 (d, J = 9.0 Hz, 4H), 1.67 (s, 6H), 1.27 (s, 36H). ^{13}C NMR (CDCl$_3$): δ 152.34, 149.32, 145.28, 144.30, 133.69, 131.96, 129.90, 129.21, 121.78, 119.24, 118.97, 117.21, 83.21, 35.09, 31.52, 23.12. ^{11}B NMR (CDCl$_3$): δ −4.7 (4B), −10.0 (16B). HRMS (FAB): m/z [M]+ Calcd for C$_{52}$H$_{79}$ClN$_2$B$_{20}$: 986.7793; Found: 986.7800.

Synthesis of 2b

This compound was prepared in a manner analogous to the synthesis of 1b using **2a** (0.67 g, 2.12 mmol), affording the title compound as a white solid (Yield: 1.22 g, 93%). ^{1}H NMR (CDCl$_3$): δ 7.32 (dd, J = 8.5, 7.3 Hz, 1H), 7.22 (s, 1H), 7.21–7.17 (m, 4H), 7.16 (s, 1H), 7.13 (d, J = 8.8 Hz, 4H), 6.88 (d, J = 1.6 Hz, 4H), 6.83 (d, J = 8.0 Hz, 2H), 1.62 (s, 6H), 1.25 (s, 36H). ^{13}C NMR (CDCl$_3$): δ 152.19, 147.71, 145.74, 145.53, 132.66, 131.66, 129.62, 129.30, 128.89, 123.47, 122.64, 121.58, 118.12, 117.86, 82.37, 35.06, 31.56, 23.20. ^{11}B NMR (CDCl$_3$): δ −4.0 (4B), −9.7 (16B). HRMS (FAB): m/z [M]+ Calcd for C$_{52}$H$_{79}$ClN$_2$B$_{20}$: 986.7793; Found: 986.7795.

Synthesis of 1

To a solution of **1b** (0.30 g, 0.30 mmol) in t-butylbenzene (20 mL) was added dropwise t-BuLi (1.6 M in pentane, 0.57 mL, 0.91 mmol) at −30 °C. After stirring at 60 °C for 2 h, pentane was removed in vacuo. Boron tribromide (0.09 mL, 0.91 mmol) was added slowly at −30 °C, and the mixture was stirred at 60 °C for 1 h. N,N-Diisopropylethylamine (DIPEA, 0.16 mL, 0.91 mmol) was added at 0 °C, and the reaction mixture was stirred at 120 °C for 12 h. After cooling down to room temperature, an aqueous solution of NaOAc was added, and the mixture was extracted with ethyl acetate (3 × 30 mL). The combined organic layer was dried over MgSO$_4$,

filtered, and washed several times with ethyl acetate. The solution was concentrated under reduced pressure, and filtered through a silica gel (eluent: dichloromethane/n-hexane = 1:5) to give a yellow solid. The product was further purified by crystallization, affording the title compound as a bright yellow solid (Yield: 0.09 g, 30%). ^{1}H NMR (CD$_2$Cl$_2$): δ 9.11 (d, J = 2.4 Hz, 2H), 7.69 (dt, J = 5.0, 2.8 Hz, 4H), 7.35 (t, J = 8.3 Hz, 1H), 7.17 (d, J = 1.7 Hz, 4H), 6.81 (d, J = 9.2 Hz, 2H), 6.26 (d, J = 8.3 Hz, 2H), 1.80 (s, 6H), 1.37 (s, 46H). ^{13}C NMR (CD$_2$Cl$_2$): δ 154.91, 149.09, 146.89, 141.12, 138.47, 133.37, 124.02, 123.24, 122.45, 118.12, 106.85, 84.22, 78.48, 35.51, 31.55, 23.49. ^{11}B NMR (CD$_2$Cl$_2$): δ 30.0 (1B), -4.1 (4B), -10.1 (16B). Anal. Calcd (%) for C$_{52}$H$_{77}$B$_{21}$N$_2$: C, 65.25; H, 8.11; N, 2.93. Found: C, 65.06; H, 7.92; N, 2.81. T_{d5} = 384 °C.

Synthesis of 2

This compound was prepared in a manner analogous to the synthesis of **1** using **2b** (0.35 g, 0.35 mmol), affording the title compound as a bright yellow solid (Yield: 0.05 g, 15%). ^{1}H NMR (CD$_2$Cl$_2$): δ 8.87 (d, J = 8.2 Hz, 2H), 7.74 (t, J = 1.6 Hz, 2H), 7.48 (dd, J = 8.2, 1.7 Hz, 2H), 7.41 (t, J = 8.3 Hz, 1H), 7.18 (d, J = 1.7 Hz, 4H), 7.01 (d, J = 1.6 Hz, 2H), 6.39 (d, J = 8.3 Hz, 2H), 1.66 (s, 6H), 1.39 (s, 36H). ^{13}C NMR (CD$_2$Cl$_2$): δ 155.30, 148.09, 147.12, 141.21, 135.50, 133.43, 133.07, 124.09, 123.24, 121.91, 121.18, 106.27, 82.81, 77.94, 35.58, 31.60, 23.50. ^{11}B NMR (CD$_2$Cl$_2$): δ 41.6 (1B), -4.9 (4B), -10.2 (16B). Anal. Calcd (%) for C$_{52}$H$_{77}$B$_{21}$N$_2$: C, 65.25; H, 8.11; N, 2.93. Found: C, 65.04; H, 8.28; N, 2.52. T_{d5} = 382 °C.

Synthesis of 3

This compound was prepared in a manner analogous to the synthesis of **1** using N^1,N^3-bis[3,5-bis(1,1,-dimethylethyl)phenyl]-2-chloro-N^1,N^3-diphenyl-1,3-benzenediamine (0.35 g, 0.35

mmol), affording the title compound as a bright yellow solid (Yield: 0.11 g, 32%). ^{1}H NMR (CD$_2$Cl$_2$): δ 8.93 (dd, J = 7.7, 1.3 Hz, 2H), 7.66 (t, J = 1.7 Hz, 2H), 7.44 (ddd, J = 8.6, 7.0, 1.6 Hz, 2H), 7.26 (dt, J = 5.8, 4.5 Hz, 3H), 6.79 (d, J = 8.6 Hz, 2H), 6.15 (d, J = 8.3 Hz, 2H), 1.37 (s, 36H).^{13}C NMR (CD$_2$Cl$_2$): δ 154.58, 148.23 , 147.37 , 141.98 , 135.23 , 132.46 , 131.32 , 124.58 , 122.62 , 120.03 , 117.67 , 105.40 , 35.50 , 31.62. ^{11}B NMR (CD$_2$Cl$_2$): δ 40.91 (1B). Anal. Calcd (%) for C$_{46}$H$_{53}$BN$_2$: C, 85.69; H, 8.29; N, 4.34. Found: C, 85.43; H, 8.35; N, 4.13. T_{d5} = 303 °C.

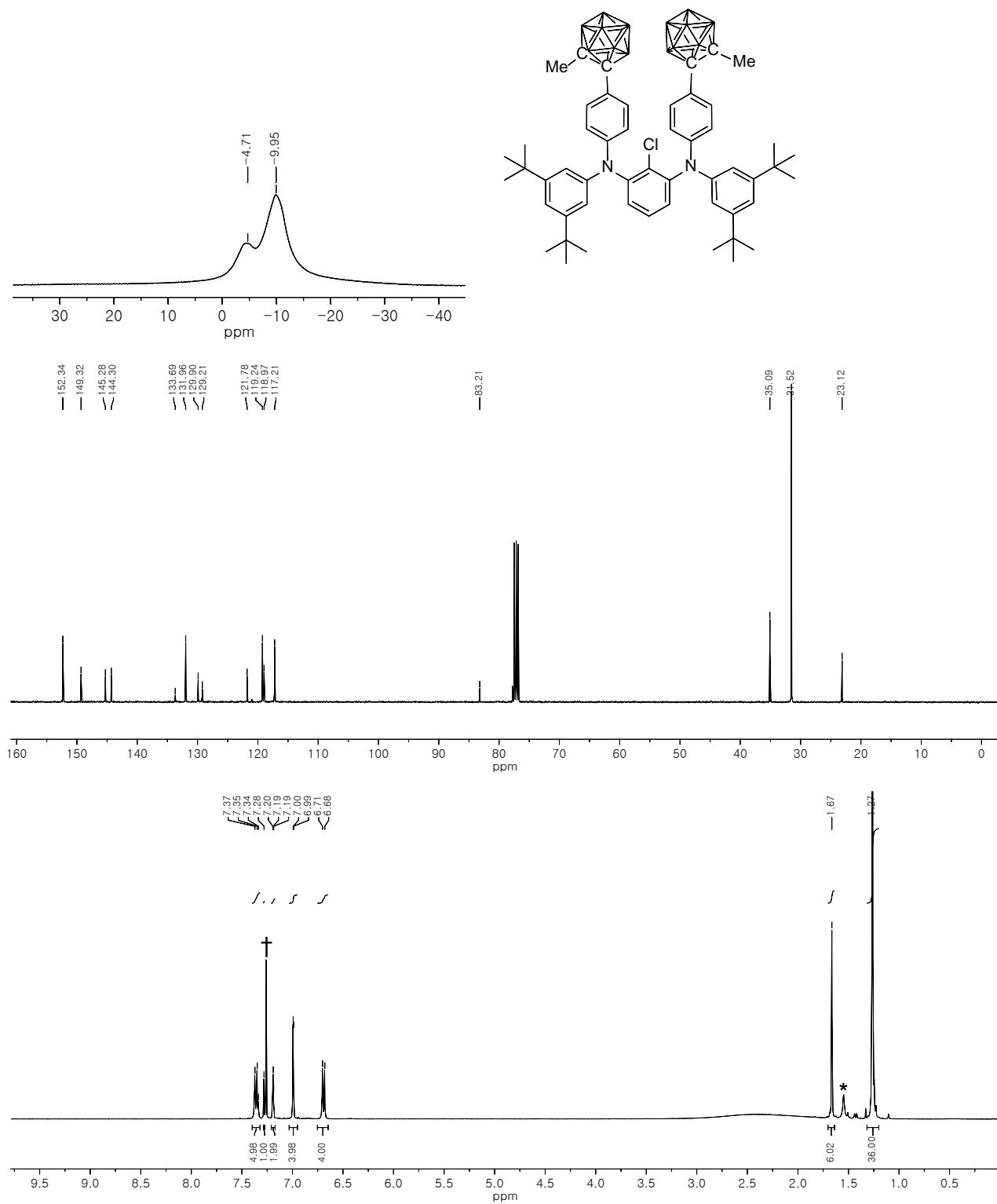**Figure 7.** ^{11}B (top), ^{13}C (middle), and ^{1}H (bottom) NMR spectra of **1b** (∗ and † from residual solvents).
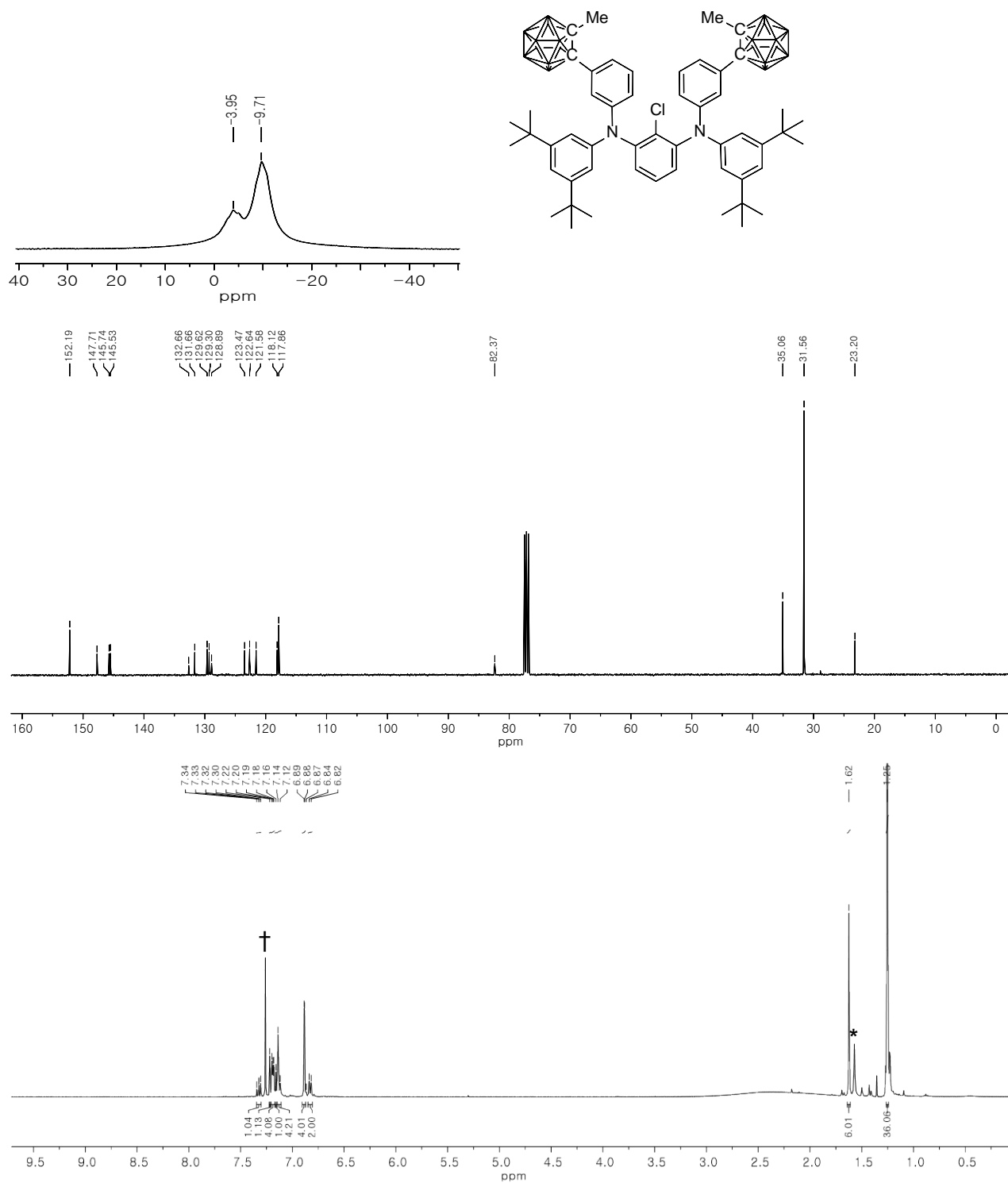
Figure 8. ^{11}B (top), ^{13}C (middle), and ^{1}H (bottom) NMR spectra of **2b** (* and † from residual solvents).
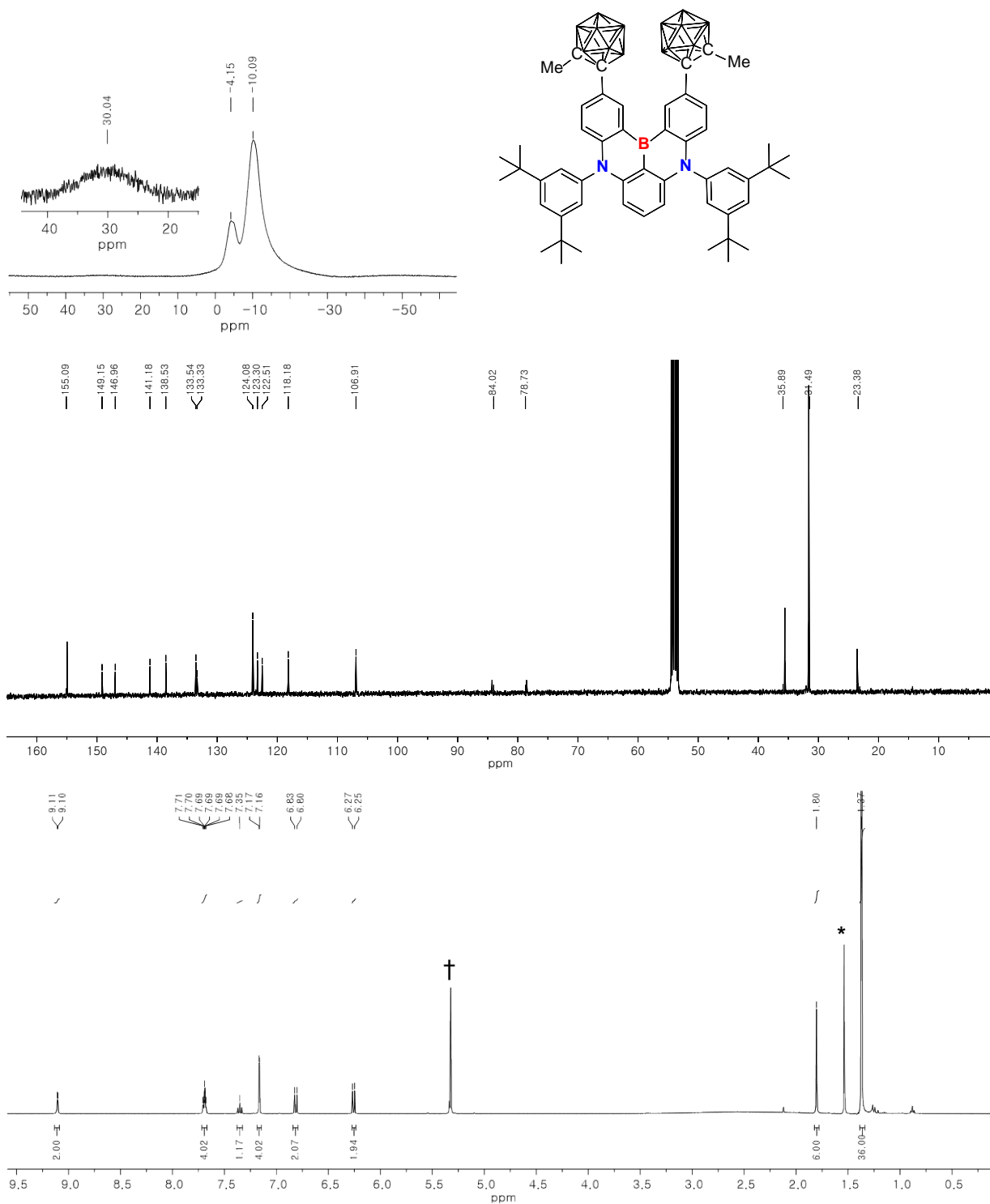
Figure 9. [11]B (top), [13]C (middle), and ^{1}H (bottom) NMR spectra of **1** (∗ and † from residual solvents).

Figure 10. ^{11}B (top), ^{13}C (middle), and ^{1}H (bottom) NMR spectra of **2** (∗ and † from residual solvents).

Figure 11. ^{11}B (top), ^{13}C (middle), and ^{1}H (bottom) NMR spectra of **3** (∗ and † from residual solvents).
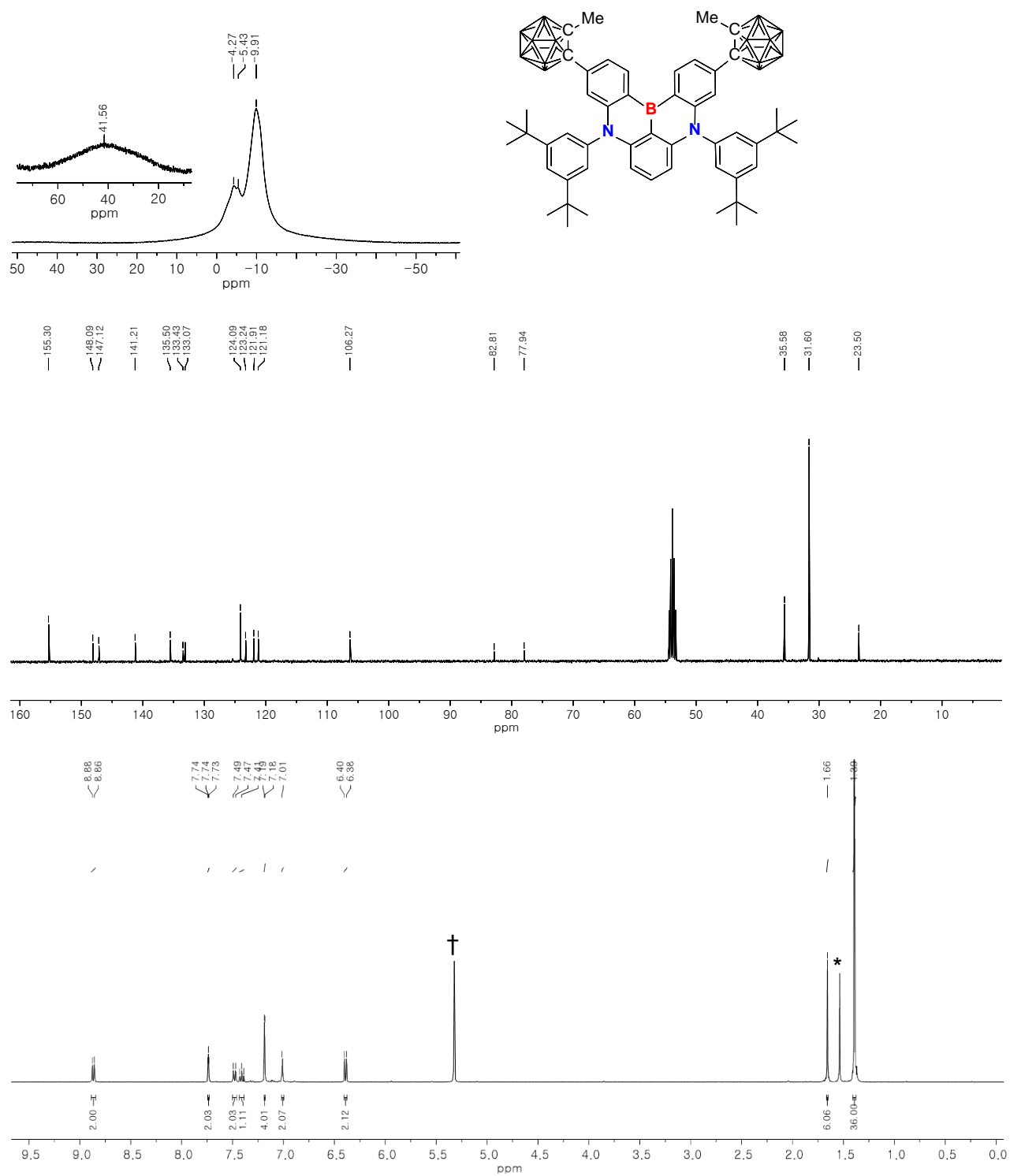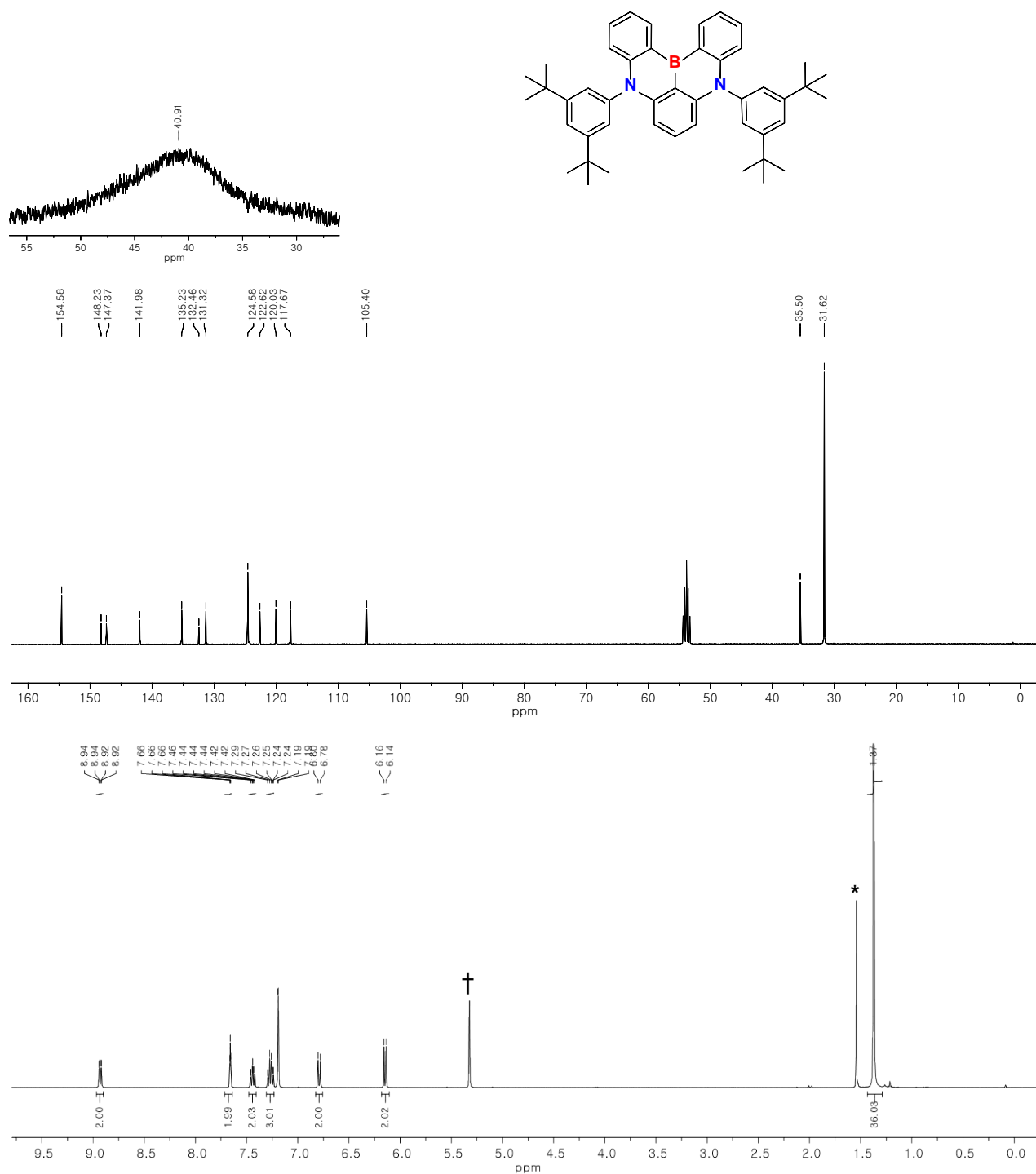
Photophcial properties

The photophysical properties of compounds **1**–**3** were initially examined in toluene (**Figure 11**a and **Table 1**). In reference **3**, a strong SRCT absorption peak was observed at 442 nm, which underwent a redshift in both **1** (451 nm) and **2** (476 nm). When compared to the HOMO and LUMO levels of **3**, determined through electrochemical oxidation and absorption onset wavelength, it was evident that carborane substitution resulted in a larger LUMO stabilization compared to HOMO stabilization. This was especially prominent in emitter **2**, where the carborane moiety is appended at the LUMO-dominating 3-position (**Figure S1**). Notably, the effect was particularly strong at the 3-position due to the inductive and conjugation effects of *o*-carborane at the para-position to the central boron atom. The FMO analysis mentioned above indicated that unlike the distinct positional electronic effects observed in previous luminophores, *o*-carborane substitution on the phenylene ring of the MR-core had a more significant impact on LUMO stabilization, resulting in an absorption band redshift.

The PL spectra of all compounds exhibited narrowband emissions, which is typical for B,N-doped MR-emitters. Similarly to the absorption, the deep blue emission peak of **3** (455 nm) experienced redshifts in **1** (467 nm) and **2** (493 nm) (**Figure 11b**). Notably, the redshift in **2** was substantial, reaching 38 nm, indicating significant stabilization of the S_1 state through carborane substitution at the **3**-position. Interestingly, no additional ICT band was observed in **1** and **2**, suggesting that the *o*-carborane moiety did not adversely affect the emissive states of the MR-core in toluene. The emission exhibited a narrow FWHM in **3** (22 nm), which was maintained in **1** (22 nm) but slightly broadened in **2** (29 nm). The high PLQY of **1** and **2** (76%−80%) were particularly noteworthy since many organic luminophores experience a significant drop in PLQY upon *o*-carborane substitution, even in toluene.[44, 55, 64] The emission lifetime confirmed the fluorescence nature of the compounds (**Table 1**). By obtaining the

fluorescence and phosphorescence peaks at 77 K, the energy gap between the S_1 and T_1 states (ΔE_{ST}) was estimated to be 0.13 eV for **1** and 0.16 eV for **2**, slightly lower than that of **3** (0.17 eV). However, no delayed fluorescence was detected in toluene, similar to typical monoboron-based MR emitters.[10]
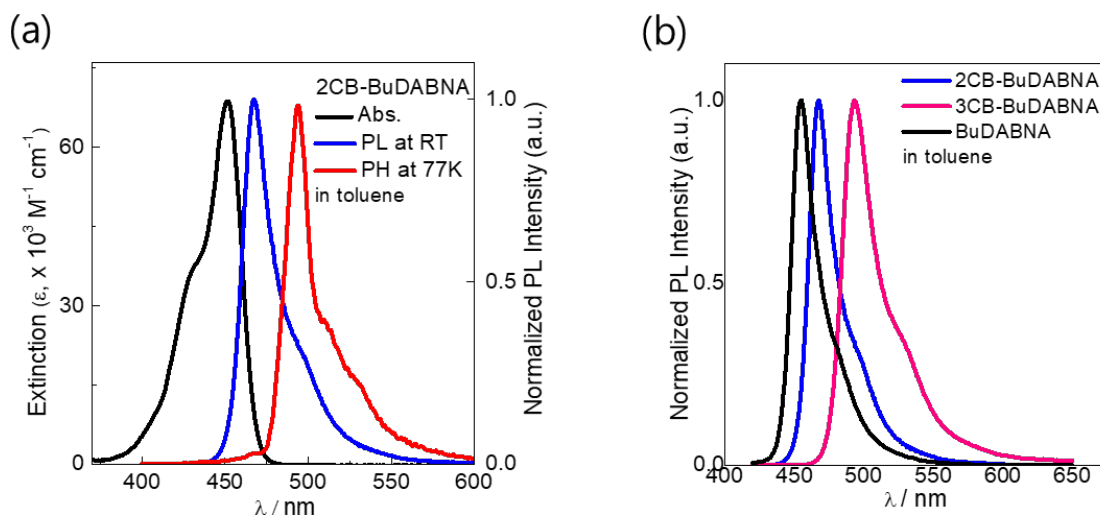

Figure 11. (a) UV/Vis absorption, PL, and phosphorescence (PH) spectra of **2CB-BuDABNA** (**1**) in toluene (2.0 × 10−5 M). (b) PL spectra of **1**, **3CB-BuDABNA** (**2**), and **BuDABNA** (**3**) in toluene.

The emission wavelengths of **1** and **2** experienced a slight red shift compared to toluene, accompanied by an increase in the FWHM. Notably, the FWHM increase was particularly pronounced in the case of **2**. However, the S_1 and T_1 energies of **1** and **2** remained comparable to those in toluene. We conducted further investigations into the emission properties of **1–3** in a rigid matrix, such as PMMA, at various doping concentrations, aiming to assess whether the steric effect of *o*-carborane prevents aggregate formation. As depicted in **Figure S3**, emitter **1** exhibited nearly the same emission peak wavelength (468 nm) as observed in toluene (467 nm), with a slight broadening in the low-energy region above 500 nm within the 5-50 wt% doping concentrations. The FWHM values also remained similar (27−30 nm). Although emitter **2**

displayed a somewhat red-shifted peak wavelength (495−501 nm), the spectral broadening and FWHM were also maintained within the 5−50 wt% doping concentrations. Notably, the PLQYs of both emitters were significantly enhanced in PMMA films (76% and 25% for 5 wt% of **1** and **2**, respectively). This indicates that the restricted rotation of the carborane moiety enhances the PLQY.[40] At high concentrations (>10 wt%), strong excimer bands above 480 nm appeared. As B,N-doped MR-emitters typically experience strong aggregation at high concentrations due to the planar MR-core, which limits their application in OLEDs to low doping concentrations, the results indicate that the methyl-*o*-carborane moieties in **1** and **2** provide substantial steric shielding effects on the MR-emitting core, enabling the use of a wide range of dopant concentrations in practical applications. Furthermore, this effect was more pronounced in **1** compared to **2**, attributed to the up and down orientations of the two methyl groups in **1**. In contrast, the methyl groups in **2** are relatively free to rotate, thus allowing for intermolecular interactions between the unprotected sides of the MR-cores to occur at high concentrations.

Table 1 Photophysical data of **1**–**3**.

Compound	λ_{abs} (nm)^a	λ_{PL} (nm) sol^a/film^b	$\Phi_{PL}{}^c$ (%) sol/film	$\Phi_p/\Phi_d{}^d$ (%) sol^a	$\Phi_p/\Phi_d{}^d$ (%) film^b	FWHM (nm)^e	$\tau_p{}^f$ (ns) sol/film	$\tau_d{}^f$ (µs) sol/film	$\Delta E_S{}^g$ (eV)	$\Delta E_T{}^g$ (eV)	$\Delta E_{ST}{}^h$ (eV)
1	451	467/468	80/76	80/–	68.3/7.7	22/27	8.35/5.97	–/50.2	2.644	2.510	0.134
2	476	493/495	76/26	76/–	25.5/0.5	29/32	9.24/5.59	–/56.4	2.515	2.375	0.157
3	442	455/455	92/75	92/–	70.4/4.6	22/29	8.26/5.68	–/94.9	2.725	2.556	0.169

a In oxygen-free toluene at 298 K (2.0×10^{-5} M). *b* 5 wt%-doped thin film in PMMA. *c* Absolute PLQYs. *d* PLQYs of prompt (Φ_p) and delayed (Φ_d) fluorescence. *e* Full width at half maximum of the PL spectrum. *f* PL lifetimes of prompt (τ_p) and delayed (τ_d) decay components. *g* Singlet (E_S) and triplet (E_T) energies estimated from the peak wavelengths of the fluorescence and phosphorescence spectra recorded at 77 K. *h* $\Delta E_{st} = E_s - E_t$

3.1.4 Results of DFT calculation

To supporting experiment results of **1**-**3** in their ground and excited states, we performed computational studies based on DFT and TDDFT at the PBE0/def2-SVP level of theory (see 3.1.2 method). The optimized ground state (S_0) structures show in **Figure 12.** In **Figure 12**, it can be observed that the HOMO is mainly distributed on the N skeleton while the LUMO is distributed on the B skeleton, indicating the characteristic of the MR-TADF molecule (**Table S2**). Additionally, compared to molecule **3**, molecules **1** and **2** exhibit a red-shift phenomenon, which is consistent with the experimental trend. The reason for the red-shift in molecules **1** and **2** is that the electron-withdrawing group carborane replaces the HOMO position in molecule **1** and the LUMO position in molecule **2**, causing the orbitals to extend to carborane (**Table S2**). As a result, the HOMO and LUMO of molecules **1** and **2** are stabilized, leading to a decrease in the HOMO-LUMO gap (E_g) and a red-shift phenomenon. Molecules have large absorption oscillator strengths, and the trend of change in ΔE_{st} value is the same as that of the experiment value which increases the **1** < **2** < **3** order.
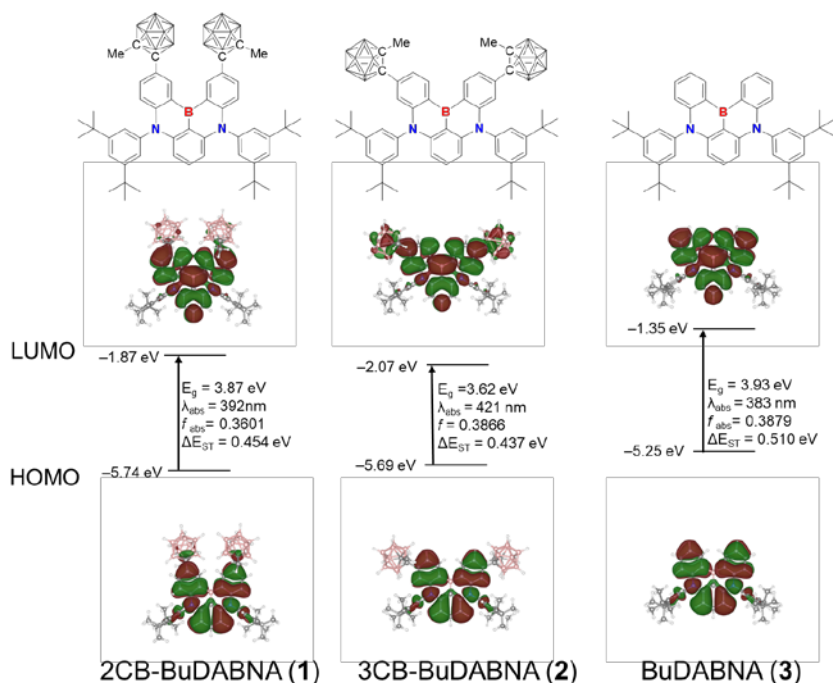

	2CB-BuDABNA (**1**)	3CB-BuDABNA (**2**)	BuDABNA (**3**)

For **1**: LUMO −1.87 eV, HOMO −5.74 eV, E_g = 3.87 eV, λ_{abs} = 392 nm, f_{abs} = 0.3601, ΔE_{ST} = 0.454 eV

For **2**: LUMO −2.07 eV, HOMO −5.69 eV, E_g = 3.62 eV, λ_{abs} = 421 nm, f = 0.3866, ΔE_{ST} = 0.437 eV

For **3**: LUMO −1.35 eV, HOMO −5.25 eV, E_g = 3.93 eV, λ_{abs} = 383 nm, f_{abs} = 0.3879, ΔE_{ST} = 0.510 eV

Figure 12. Frontier molecular orbitals of **1**, **2**, and **3** (isovalue = 0.01 e/Å^3) at their ground state (S$_0$) geometries optimized using PBE0/def2-SVP calculations. Numerical data are provided for MO energies, absorption wavelength (λ_{abs}), absorption oscillator strengths (f_{abs}) HOMO–LUMO gaps (E_g), and S$_1$–T$_1$ energy gap (ΔE_{ST}).

3.1.5 Conclusion

In order to observe photophysical and physical properties different from conventional *o*-carborane, we conducted research by replacing MR-TADF molecules with *o*-carborane. When *o*-carborane was substituted into the MR-TADF molecule, unlike the existing chromophore of *o*-carborane, it was found that light came out from the MR core through the absence of a broad band of ICT. The synthesized molecules undergo a redshift, which was explained to be due to carborane through computational studies.

3. 2. Computational study on Donor-Acceptor TADF

3.2.1 Introduction

The photophysical properties of three donor-acceptor-type thermally activated delayed fluorescence (TADF) emitters (**PXZBAO** (**1**), **PXZBTO** (**2**), and **PXZBPO** (**3**)) are herein investigated using TDDFT calculations, which were comprising a phenoxazine (PXZ) donor and differently π-expanded boron-carbonyl (BCO) hybrid acceptor units. Photoluminescence experiments revealed that the emitters exhibit the red (**1**) to orange (**3**) emissions with an increase in the π-expansion in the BCO acceptors. This unusual emission color shift can be explained by the LUMO energy level of TADF emitter, which is attributed to the strength of local aromaticity for the π-expanded unit of BCO acceptors, for which the squared effective ring electron density ($ERED^2$) was evaluated as a descriptor for the local aromaticity of a ring over all Kekulé structures based on WFRT analysis. Also, To provide photophysical insights of their TADF processes, we evaluated the SOCME between the S_1 and T_n ($n = 1$ and 2) excited states. The SOCME between the S_1 and T_2 states is much larger than that between the corresponding S_1 and T_1 states for all compounds, as expected by El-Sayed rule. Consequently, all the emitters exhibit strong spin-orbit coupling between their T_2 and excited singlet (S_1) states, leading to a fast reverse intersystem crossing with rate constants of ~$10^6 \, s^{-1}$. We believe that our study will be useful for the design of D−A-type TADF emitters with fast RISC and controlled photophysical properties.

According to the El-Sayed rule, SOC interaction is allowed between the ^1CT and locally excited triplet state (^3LE). [13] Therefore, allocating a proper ^3LE state, as an energetically close-lying T_n state to the ^1CT (S_1) state, could be a viable route to enhance SOC in D−A-type TADF emitters.[80-83] It has been demonstrated that the RISC rate can be significantly boosted by the

strong SOC between the ^{1}CT and ^{3}LE (T$_2$) states[84-88], which is preceded by vibronic coupling between the ^{3}CT (T$_1$) and ^{3}LE (T$_2$) states.[80, 88-90] As a result, the very fast RISC rates of over 10^7 s^{-1} have been recently achieved by Kaji and Yasuda groups, which in turn resulted in the low efficiency roll-offs of the TADF-OLEDs.[86, 91]

To activate a ^{3}LE state, $^3\pi\pi*$ states of organic D or A units have been typically considered in the D−A-type TADF emitters. However, the $^3\pi\pi*$ state is hardly accessible in some cases, such as the acceptors in boron-based TADF emitters owing to the dominant π (Ar) to π (B) CT excited state character of the typical triarylboryl acceptors. Alternatively, the ^{3}n$\pi*$ state could be another option for activating a ^{3}LE state since it can be accessible in heteroatom-containing molecules.[9, 11] In particular, TADF emitters with aryl carbonyl acceptors opened a way to exhibit short-lived delayed fluorescence using the carbonyl-centered ^{3}n$\pi*$ state in the T$_1$ state, boosting the RISC process.[9] For example, boron−carbonyl (BCO) hybrid acceptor, in which a carbonyl group is incorporated into the cyclic triarylboron, namely, *B*-heterotriangulene, effectively activated the ^{3}LE state. [9, 11]The ^{3}n$\pi*$ state of the dibenzo-BCO (BAO) acceptor is located at the T$_2$ level of the emitters, inducing strong SOC with the ^{1}CT (S$_1$) state. Consequently, the fast RISC rate constants exceeding 10^6 s^{-1} and short delayed fluorescence lifetimes of ca. 1 μs were achieved[11], resulting in TADF-OLEDs with high efficiencies and low-efficiency roll-offs. The main advantage of the TADF emitter with the BCO acceptor is that the ^{3}LE state in the BCO acceptor can be effectively adjusted by the π-skeleton of the *B*-heterotriangulene unit. In other words, the high-lying lone electron pairs of oxygen atoms could compete with the π-orbitals of the neighboring aryl systems, compromising the ^{3}n$\pi*$ state with the $^3\pi\pi*$ state of the BCO acceptor. Using the strategy, we can access diverse SOC processes among ^{1}CT, ^{3}n$\pi*$, and $^3\pi\pi*$ states to achieve efficient RISC.

3.2.2 Method

To investigate the transition properties for the RISC processes for three D−A compounds, **1**, **2** and **3**, we carried out the computational study based on the TDDFT. The PBE0 hybrid functional[76] and 6-31G(d,p) basis set implemented in GAUSSIAN 16 software package were used to obtain their geometric, electronic, and optical properties.[77] Their ground (S_0) states of compounds were optimized using DFT calculations, and their lowest singlet (S_1) and two triplet (T_1 and T_2) excited states were optimized using TDDFT calculations with the same functional and basis set. The polarizable continuum model using the integral equation formalism (IEFPCM) was employed to take account for the influence of solvent medium (toluene) on molecular geometric and electronic structures. [78] Natural transition orbital analysis was performed to characterize the excited states, i.e., CT and LE.[9, 11] The NTO analysis and the overlap integral extents between frontier molecular orbitals, HOMO and LUMO, were computed using Multiwfn programs[101]. The transition characteristics of the pristine donor (PXZH) and acceptor (HBAO, HBTO, and HBPO) molecules were also elucidated using NTO analysis to rationalize the combination of donor and acceptor moieties. The non-radiative decay rate for RISC processes, i.e., $S_1 \leftarrow T_n$ (n = 1 and 2), were evaluated via thermal vibrational correlation function (TVCF) approach in Molecular Materials Property Prediction Package (MOMAP 2020B), which has been successfully utilized to predict the photophysical properties of a wide range of luminescent molecules.[9, 11] The TVCF formalism is derived from Fermi's golden rule and second-order perturbation combining both non-adiabatic coupling and SOC as well as considering mode-mixing (Duschinsky rotation effect) and the coordinate-dependent transition dipole (Herzberg-Teller effect). SOCME, described with Breit-Pauli Hamiltonian, between excited S_1 and T_n (n = 1 and 2) were computed by using the quadratic response function with PCM method implemented in Dalton2018,[100] in which the B3LYP hybrid

functional[102] and 6-31G(d,p) basis set were used. Wave-function-based resonance theory (WFRT) analysis based on Fries rule was performed using EzReson program,[103] which was recently developed to explain the local aromaticity of rings based on possible Kekulé structures via estimating the squared effective ring electron density (ERED^2) as a descriptor for the local aromaticity of a ring.[12]

3.2.3 Experimental phonemes: controlling local triplet excited states and unusual color change.

The PL spectra of **1**–**3** exhibit structureless emissions in the red-to-orange regions, indicating that typical ICT emission occurred (**Figure 13c**). The emission wavelength is gradually blue-shifted from 1 to 3 (λ_{PL} = 619 nm for **1**, 597 nm for **2**, 574 nm for **3**), which is the same trend as their low-energy absorptions. Interestingly, the PLQY of the compounds increased with the increasing number of the naphthyl rings in the BCO acceptors; whereas compound **1** showed a low PLQY of 29%, the PLQYs of **2** and **3** reached 63% and 79%, respectively. The transient PL decays show prompt and delayed components of the emissions (**Figure 13d**).
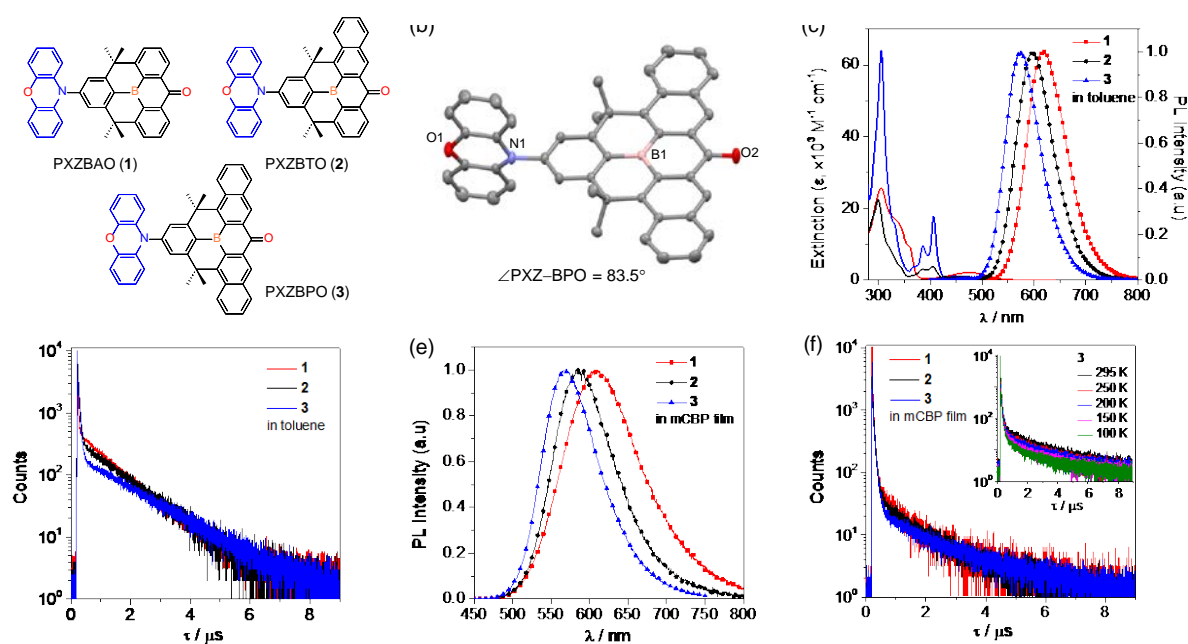
Figure 13. (a) Chemical structures of **1–3**. (b) X-ray crystal structure of **3**. (c) UV/Vis absorption (left) and PL (right) spectra of **1–3** in toluene (2.0×10^{-5} M). (d) Transient PL decays of **1–3** in toluene at 298 K. (e) PL spectra of **1–3** in 5 *wt.*%-doped mCBP (3,3′-di-(9*H*-carbazol-9-yl)-1,1′-biphenyl) host films. (f) Transient PL decays of the mCBP host films doped with 5 *wt.*% of **1–3** at 298 K. Inset: Temperature-dependent transient PL decay of **3** in a doped host film.

Notably, the delayed fluorescence lifetimes (τ_d) were very short for all compounds (1.04–1.57 μs) comparable to those found in previous BAO-containing compounds[11] and showed an increasing tendency on going from **1** to **3**. All compounds exhibited broad fluorescence and phosphorescence spectra at 77 K, indicating the CT excited state characteristics. The resulting S_1–T_1 energy gaps (ΔE_{ST}) were very small for **1–3** (ΔE_{ST} = 11–47 meV), which was in line with the short-lived delayed fluorescence of **1–3**. The photophysical properties of the doped mCBP (3,3′-di(9*H*-carbazol-9-yl)-1,1′-biphenyl) host films with 5 *wt.*% of **1–3** were further investigated (**Figure 13e** and **Table 2**). All films show red-to-orange emissions (λ_{PL} = 568–609 nm) with slight rigidochromic blue shifts compared with the emissions in the solution state. The PLQYs of the film samples also increase in the order **1** < **2** < **3**, similar to the results obtained in solution. Transient PL decay traces, with their temperature dependence behavior, indicate that TADF characteristics with short-lived delayed fluorescence (τ_d = 1.03–1.76 μs) are retained in the film state (**Figure 13f**). The delayed fluorescence lifetimes are also in the same order as the solutions. To gain further insight into the excited state dynamics, the rate constants of the radiative decay (k_r), intersystem crossing (k_{ISC}), and k_{RISC} were determined (**Table 2**).[9, 11] The values are high and are in the order of ~10^6, and ~10^6 s^{-1}, respectively. In particular, the k_{RISC} values of ~10^6 s^{-1}, which are inversely proportional to the delayed fluorescence lifetimes of **1–3**, are comparable to those of the TADF emitters showing a fast RISC, [88, 95] including previous BAO-containing

compounds.[11] It is noteworthy that the nonradiative decay rate constant in the S_1 ($k_{nr,S}$) excited state of **1** is very high ($>10^7$ s^{-1}) and is even more significant than the k_r value. This finding indicates that the high $k_{nr,S}$ is mainly responsible for the low PLQY of the red emitter **1**, as dictated by the energy gap law.[96-97] In contrast, **2** and **3**, with shorter-wavelength emissions, exhibited smaller $k_{nr,S}$ values than their k_r values.

Table 2. Photophysical data and rate constants of compounds.

Compound	λ_{abs} (nm)[a]	λ_{PL} (nm) sol[a]/film[b]	FWHM (nm)[a,c]	$\Phi_{PL}{}^d$ (%) sol/film	$\tau_p{}^e$ (ns) sol/film	$\tau_d{}^e$ (μs) sol/film	$\Delta E_{ST}{}^{a,f}$ (meV)	$k_r{}^{b,g}$ (10^6 s^{-1})	$k_{nr,S}{}^{b,g}$ (10^6 s^{-1})	$k_{ISC}{}^{b,g}$ (10^6 s^{-1})	$k_{RISC}{}^{b,g}$ (10^6 s^{-1})
PXZBAO (**1**)	476	619/609	90	29/45	25.3/38.7	1.04/1.03	11	9.04	11.1	5.74	1.25
PXZBTO (**2**)	465	597/586	84	63/52	46.1/56.4	1.21/1.45	14	6.91	6.38	4.43	0.92
PXZBPO (**3**)	457	574/568	78	79/68	54.6/57.8	1.57/1.76	47	8.48	3.99	4.83	0.79

a In oxygen-free toluene at 298 K (2.0 × 10−5 M). *b* In 5 wt.%-doped films in an mCBP host. *c* Full width at half maximum. *d* Absolute PLQYs. *e* Lifetimes of prompt (τ_p) and delayed (τ_d) PL decay components. *f* Singlet–triplet energy gaps from the fluorescence and phosphorescence spectra at 77 K. *g* k_r, $k_{nr,S}$, k_{ISC}, and k_{RISC} are the rate constants of fluorescence radiative decay, nonradiative decay at S_1 state, intersystem crossing, and RISC, respectively.

3.2.4 Results of DFT calculation

To elucidate the photophysical and electronic properties of **1**–**3** in their ground and excited states, we performed computational studies based on DFT and TDDFT at the PBE0/6-31G(d,p) level of theory (see Method 3.2.2). The optimized ground state (S_0) structures shown in **Figure 14** exhibit the large dihedral angles (θ) of 82°−88° between the PXZ donor and BCO acceptor units in all compounds, which are comparable to that observed in the crystal structure of **3**. The orthogonal D−A alignment leads to the well-separated HOMOs and LUMOs localized on the D and A units, respectively. Note that the LUMOs are spread out on the entire BCO acceptor units. Notably, the HOMO−LUMO gaps (E_g) increase in the order of **1** < **2** < **3** owing to the gradual elevation of the acceptor-centered LUMO level. Indeed, the theoretical LUMO levels of the BCO acceptor molecules showed the same tendency (**Figure S4**). This finding is in accordance with the trend observed in the experimental absorption and emission. The negligible ΔE_{ST} values (3−4 meV) are similar to the experimental results.
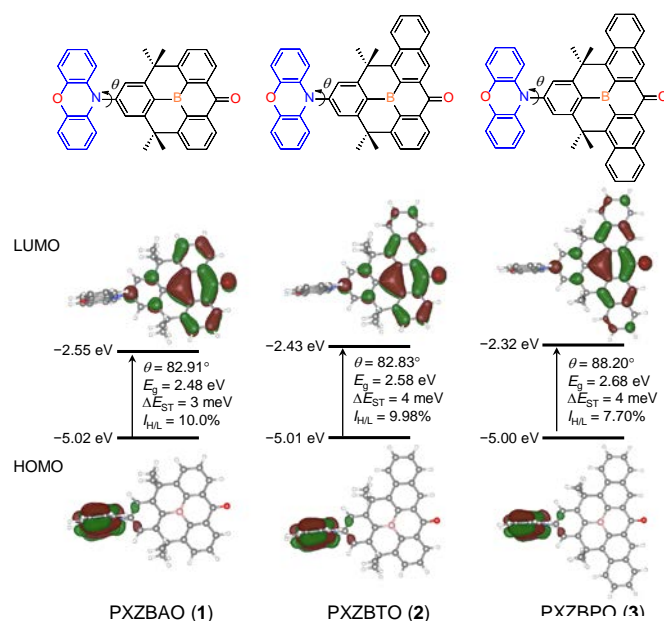
Figure 14. Frontier molecular orbitals of PXZBAO (**1**), PXZBTO (**2**), and PXZBPO (**3**) (isovalue = 0.03 e/Å^3) at their ground state (S_0) geometries optimized using PBE0/6-31G(d,p) calculations. Numerical data are provided for MO energies, dihedral angles (θ) between donor and accepter moieties, HOMO−LUMO gaps (E_g), S_1−T_1 energy gap (ΔE_{ST}), and overlap integrals between

HOMO and LUMO ($I_{H/L}$).

Next, to explain the unusual color shift and elevation of the LUMO level with the increase of the π-expansion in the BCO acceptors, we carried out the wave-function-based resonance theory (WFRT) analysis based on Fries rule, which was recently developed for evaluating the local aromaticity of rings based on possible Kekulé structures (see Method 3.1.2).[12] The local aromaticity analysis was carried out using the model compounds corresponding to the moieties of linearly fused aromatic rings including boron atom and carbonyl group in BCO acceptors to identify how the π-expansion influences their overall aromaticity (**Figure 15**). The linearly fused rings dominantly contribute to the LUMO distribution of D–A compounds as confirmed by DFT calculations above (**Figure 14**), and their π-conjugated degree can be influenced by the local aromaticity of central ring including boron atom and carbonyl group. As observed in our experiment, the LUMO level of model compounds is gradually destabilized as the number of phenyl ring increases (see **Table S2**). This distinguished behavior of LUMO level despite the π-expansion is expected to be highly related with the local aromaticity of the central ring based on the LUMO distribution of model compounds compared with their HOMO distribution (**Figure S5**). Therefore, the squared effective ring electron density ($ERED^2$) was evaluated as a descriptor for the local aromaticity of a ring over all Kekulé structures based on WFRT analysis (**Figure S6**), where a larger $ERED^2$ value indicates a higher aromaticity.[12] The estimated $ERED^2$ value of the central ring gradually decreases from 0.50 to 0.24 as the π-conjugated network is expanded (**Figure 15**), and thus the reduced aromatic character of LUMO would be responsible to the destabilization of LUMO level as observed in the experiment. In addition, we also examined the influence of heteroatom on the local aromaticity of the central ring and further on the LUMO energy by changing B–H moiety with N–H. However, the substitution

51

with N–H results in a conventional feature due to π-expansion, i.e., the stabilization of LUMO level, which can be understood with the slightly increased ERED^2 value (**Table S2**).
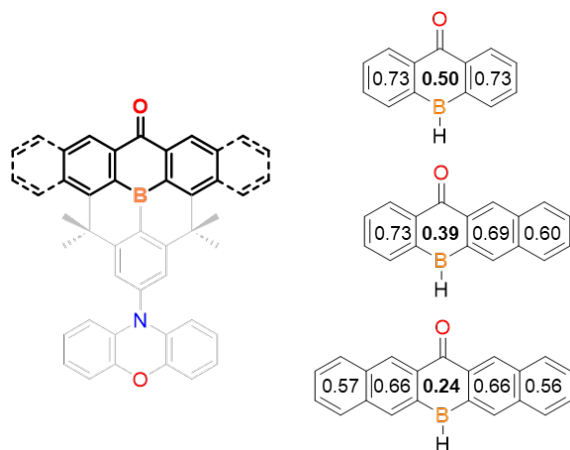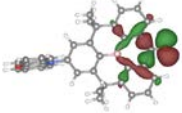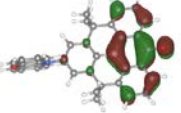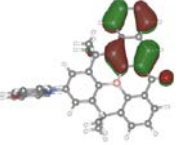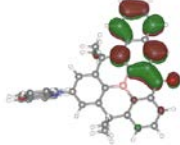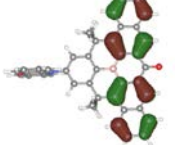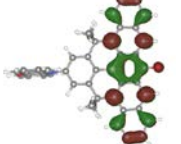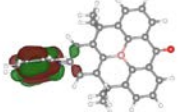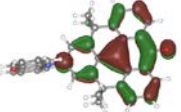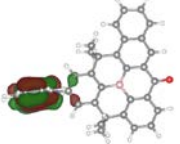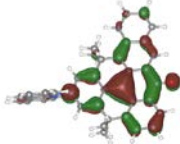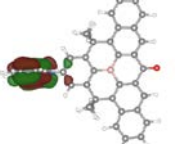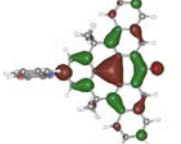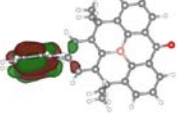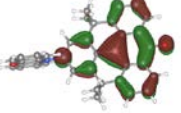

Figure 15. Local aromaticity analysis for the model compounds corresponding to the moieties of linearly fused aromatic rings including boron and carbonyl group in BCO acceptors. The wave-function-based resonance theory (WFRT) based on Fries rule was employed to estimate the square of effective ring electron density (ERED2) as a descriptor of local aromaticity for the Kekulé structure of the most dominant resonator, for which the wavefunctions obtained at PBE0/6-31G(d,p) level of theory were used.
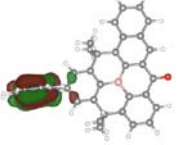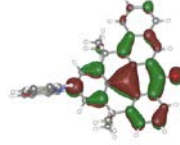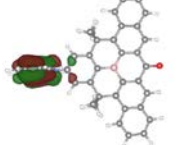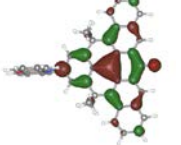
Finally, the natural transition orbitals (NTOs) of **1−3** were analyzed to examine the lowest-energy and upper-lying excited states (**Table 3**). In all compounds, the S_1 and T_1 states arise from the D-to-A CT transition, which is the same as the fluorescence and phosphorescence features of the compounds. The T_2 states of all compounds are assignable to a BCO acceptor-centered, locally excited triplet (^3LE_A) state. Remarkably, while the ^3LE_A state of **1** has a $^3n\pi^*$ character as observed in previous BAO-containing compounds,[11] compounds **2** and **3** based on naphtho-fused BTO and BPO acceptors show different features of their ^3LE_A states. In both compounds, the particle NTOs are contributed from the carbonyl π^* orbital to some extent. However, the hole NTOs have insignificant contributions from the lone pairs of the oxygen atom. This finding indicates that the ^3LE_A states of **2** and **3** are the best assigned to a naphthyl-centered $^3\pi\pi^*$ state. It is likely that the increased π-conjugation in the naphthyl ring renders the lowest-lying $^3\pi\pi^*$ state more stable than

the $^3n\pi*$ in **2** and **3** (**Figure S7**).[98] To support this experimentally, we measured the phosphorescence of the BCO acceptor molecules. The spectra exhibited vibronic progressions corresponding to the $^3n\pi*$ or $^3\pi\pi*$ state, and the T_1 state of the BCO acceptors ($E_T = 2.41$–2.75 eV) was lower in energy than that of the PXZ donor ($E_T = 2.79$ eV).[99] The NTOs of the individual acceptor molecules further indicate that the T_1 states of the acceptors have the same NTO features as those of the T_2 (^3LE_A) states of **1**–**3** (**Figure S8**). Along with the vanishingly small ΔE_{ST}, it can be thus inferred from these findings that the RISC in **1**–**3** could be facilitated by strong SOC between the T_2 (^3LE_A) and S_1 (^1CT) states.[89, 92] To confirm it, we calculated the SOCMEs between the S_1 and T_n ($n = 1$ and 2) excited states (**Table 3**).[100] The SOCME between the S_1 and T_2 states ($<^1CT|\hat{H}_{SOC}|^3LE>$) is much larger than that between the corresponding S_1 and T_1 states ($<^1CT|\hat{H}_{SOC}|^3CT>$) for all compounds, as expected by El-Sayed rule. In fact, the latter SOC was negligibly small. Thus, this result implies an acceleration of the RISC process by the strong SOC between the ^1CT and ^3LE states in **1**–**3**. Note that the internal conversion (IC) process between T_1 and T_2 is expected to be highly fast compared with ISC and RISC because the non-adiabatic vibronic coupling between T_1 and T_2 was reported to be tens or hundreds of times larger than spin-orbit coupling between S_1 and low-lying triplet states.[95] A further evaluation of the non-radiative decay rate constants for RISC processes, i.e., $T_n \rightarrow S_1$,[9, 11] led to the T_2 to S_1 RISC rate constants ($k_{T_2 \rightarrow S_1}$) of ca. $10^5 \sim 10^6$ s^{-1} that are greater than the corresponding T_1 to S_1 rate constants ($k_{T_1 \rightarrow S_1}$). The $k_{T_2 \rightarrow S_1}$ values also positively correlated with the SOC, showing the values in the order of **1** > **2** > **3**, which qualitatively follow the same trend as the experimental k_{RISC} values in **Table 2**.

Table 2. Natural transition orbitals (NTOs) of compounds **1**–**3** for the transitions from the S0 state to the S_1, T_1, and T_2 states obtained using the TDDFT calculations at the PBE0/6-31G(d,p) level of theory. The adiabatic excitation energies are given in parentheses. ^{3}LEA denotes the locally excited triplet state at the acceptor moiety. The calculated spin-orbit coupling matrix elements and transition rates for the RISC processes between the S1 and Tn (n = 1 and 2) states at 298 K are also provided.
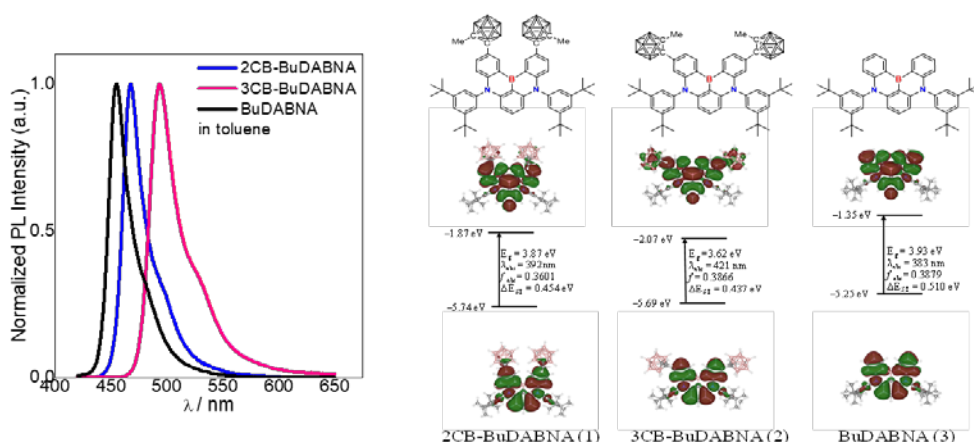
1	Hole	Particle	**2**	Hole	Particle	**3**	Hole	Particle
T_2 (^{3}LE$_A$) (2.412 eV)			T_2 (^{3}LE$_A$) (2.094 eV)			T_2 (^{3}LE$_A$) (2.060 eV)		
T_1 (^{3}CT) (1.770 eV)			T_1 (^{3}CT) (1.885 eV)			T_1 (^{3}CT) (1.996 eV)		
S_1 (^{1}CT) (1.774 eV)			S_1 (^{1}CT) (1.888 eV)			S_1 (^{1}CT) (2.000 eV)		
$\langle S_1|\hat{H}_{SOC}|T_1\rangle$	0.007 cm^{-1}		$\langle S_1|\hat{H}_{SOC}|T_1\rangle$	0.032 cm^{-1}		$\langle S_1|\hat{H}_{SOC}|T_1\rangle$	0.007 cm^{-1}	
$\langle S_1|\hat{H}_{SOC}|T_2\rangle$	0.141 cm^{-1}		$\langle S_1|\hat{H}_{SOC}|T_2\rangle$	0.125 cm^{-1}		$\langle S_1|\hat{H}_{SOC}|T_2\rangle$	0.058 cm^{-1}	
$k_{T_1 \to S_1}$	4.81×10^4 s^{-1}		$k_{T_1 \to S_1}$	7.55×10^5 s^{-1}		$k_{T_1 \to S_1}$	5.42×10^4 s^{-1}	
$k_{T_2 \to S_1}$	1.38×10^6 s^{-1}		$k_{T_2 \to S_1}$	7.83×10^5 s^{-1}		$k_{T_2 \to S_1}$	1.60×10^5 s^{-1}	

3.2.5 Conclusion

This unusual emission color shift can be explained by the LUMO energy level of TADF emitter, which is attributed to the strength of local aromaticity for the π-expanded unit of BCO acceptors, for which the squared effective ring electron density ($ERED^2$) was evaluated as a descriptor for the local aromaticity of a ring over all Kekulé structures based on WFRT analysis. Also, To provide photophysical insights of their TADF processes, we evaluated the SOCME between the S_1 and T_n (n = 1 and 2) excited states. The SOCME between the S_1 and T_2 states is much larger than that between the corresponding S_1 and T_1 states for all compounds, as expected by El-Sayed rule. Consequently, all the emitters exhibit strong spin-orbit coupling between their T_2 and excited singlet (S_1) states, leading to a fast reverse intersystem crossing with rate constants of ~10^6 s^{-1}. We believe that our study will be useful for the design of D–A-type TADF emitters with fast RISC and controlled photophysical properties.

4. Conclusion

1. In our research, we aimed to explore novel spectroscopic and physical properties by substituting *o*-carborane into MR-TADF molecules, as an alternative to conventional *o*-carborane. Through this substitution, we made an interesting discovery: unlike the existing chromophore of *o*-carborane, the presence of *o*-carborane led to the emission of light from the MR core without the presence of a broad band of ICT. Computational studies revealed that the synthesized molecules exhibited a redshift, which was attributed to the influence of carborane. Additionally, the presence of carboranes caused a reduction in the PLYQ in various media. This effect can be attributed to the alteration in the $C_{CB}-C_{CB}$ length difference of *o*-carborane and the rotational behavior of *o*-carborane.

2. Unusual emission color shift can be explained by the LUMO energy level of TADF emitter, which is attributed to the strength of local aromaticity for the π-expanded unit of BCO acceptors, for which the squared effective ring electron density ($ERED^2$) was evaluated as a descriptor for the local aromaticity of a ring over all Kekulé structures based on WFRT analysis. Also, To provide photophysical insights of their TADF processes, we evaluated the SOCME between the S_1 and T_n (n = 1 and 2) excited states. The SOCME between the S_1 and T_2 states is much larger than that between the corresponding S_1 and T_1 states for all compounds, as expected by El-Sayed rule. Consequently, all the emitters exhibit strong SOCME between their T_2 and excited singlet (S_1) states, leading to a fast

reverse intersystem crossing with rate constants of $\sim 10^6$ s^{-1}. We believe that our study will be useful for the design of D−A-type TADF emitters with fast RISC and controlled photophysical properties.
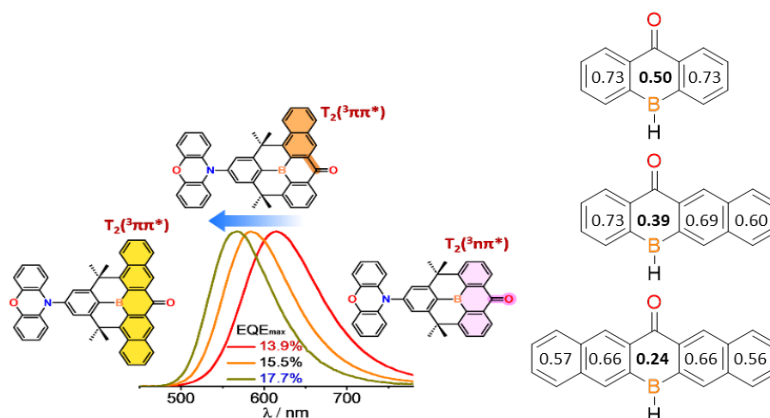
5. Supporting information

Cyclic Voltammetry

Cyclic voltammetry measurements were carried out in CH_2Cl_2 (5×10^{-4} M) with a three-electrode cell configuration consisting of platinum working and counter electrodes and a $Ag/AgNO_3$ (0.01 M in CH_3CN) reference electrode at room temperature. Tetra-n-butylammonium hexafluorophosphate (0.1 M) was used as the supporting electrolyte. The redox potentials were recorded at a scan rate of 100 mV/s and are reported with reference to the ferrocene/ferrocenium (Fc/Fc+) redox couple. The HOMO energy levels were determined from the electrochemical oxidation ($E_{1/2}$) peaks of cyclic voltammograms while the LUMO energy levels were estimated from the optical band gap (E_g) and the HOMO levels.
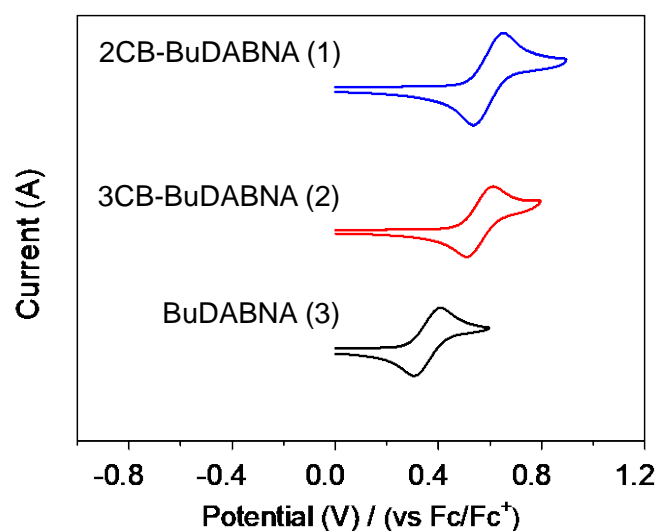
	E_g (eV)[a]	E_{ox} (V)[b]	E_{HOMO} (eV)	E_{LUMO} (eV)
1	2.65	0.59	−5.39	−2.75
2	2.50	0.56	−5.36	−2.91
3	2.71	0.36	−5.16	−2.44

Figure S1. Cyclic voltammograms of 2CB-BuDABNA (**1**), (b) 3CB-BuDABNA (**2**), and (c) BuDABNA (**3**) showing oxidation (1.0×10^{-3} M in CH_2Cl_2, scan rate = 100 mV/s).

Thermogravimetric Analyzers
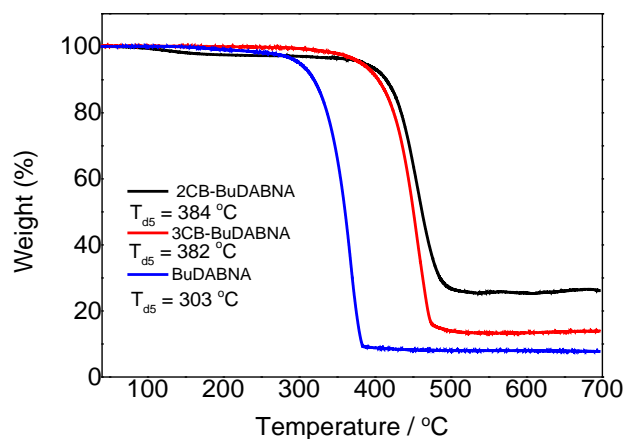
Figure S2 TGA curves of 2CB-BuDABNA (**1**), (b) 3CB-BuDABNA (**2**), and (c) BuDABNA (**3**).
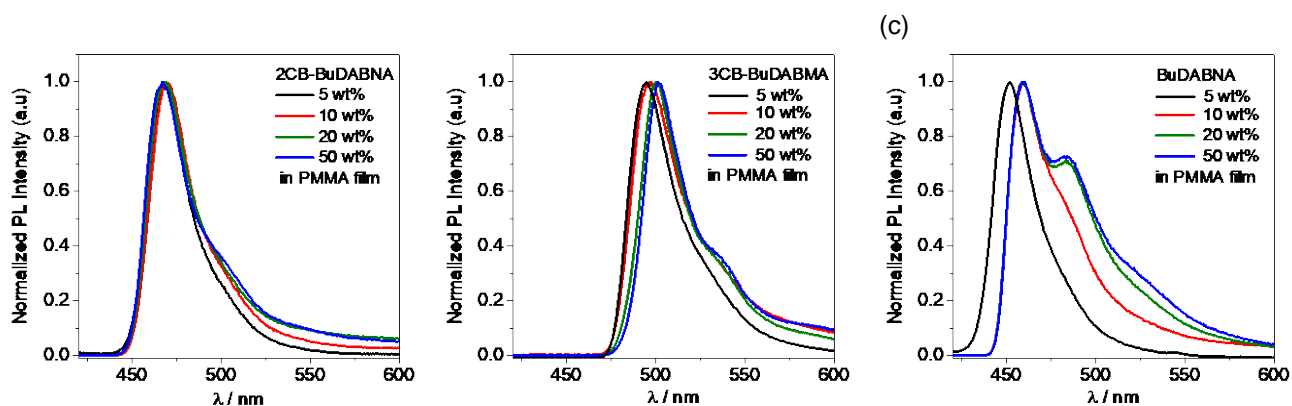
	2CB-BuDABNA			3CB-BuDABNA			BuDABNA		
wt% in PMMA	λ_{em} (nm)	PLQY (%)	FWHM (nm)	λ_{em} (nm)	PLQY (%)	FWHM (nm)	λ_{em} (nm)	PLQY (%)	FWHM (nm)
5	468	76	27	495	25	32	452	75	29
10	469	53	29	497	21	35	459	35	37
20	468	22	30	500	18	30	459	34	48
50	467	16	30	501	18	29	459	14	51

Figure S3. PL spectra and photophysical data of PMMA films doped with various concentrations of (a) 2CB-BuDABNA (**1**), (b) 3CB-BuDABNA (**2**), and (c) BuDABNA (**3**).

Table S1. HOMO and LUMO contributaion of 2CB-BuDABNA (**1**), (b) 3CB-BuDABNA (**2**), and (c) BuDABNA (**3**)

		HOMO-part	LUMO-part	CB	other
2CB-BuDABNA	HOMO	84.5	9.91	2.54	3.06
	LUMO	22.1	73.2	3.50	1.26
3CB-BuDABNA	HOMO	85.8	10.4	0.59	3.17
	LUMO	24.4	63.5	10.9	1.30
BuDABNA	HOMO	86.2	10.7	-	3.06
	LUMO	21.5	77.0	-	1.51
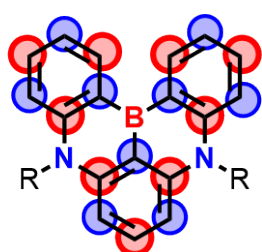
Blue: HOMO part
Red: LUMO part
CB: Me-carborane

.

LUMO

−2.40 eV

−2.29 eV

−2.18 eV
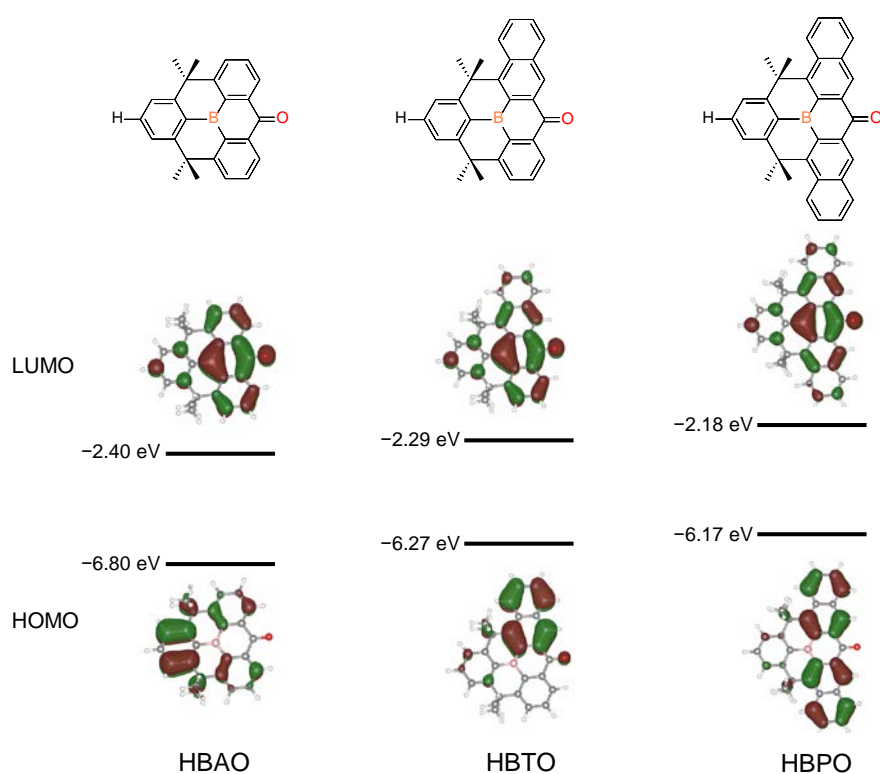
−6.80 eV

−6.27 eV

−6.17 eV

HOMO

HBAO   HBTO   HBPO

Figure S4. Frontier molecular orbitals of acceptor molecules, HBAO, HBTO, and HBPO

(isovalue = 0.03 e/Å^3) at their ground state (S$_0$) geometries from PBE0/6-31G(d,p) calculations.

Table S2. HOMO and LUMO energies (eV), their gap (E_g, eV), and the square of effective ring electron density (ERED^2) as a descriptor of local aromaticity for the central ring including X group.

X	E(HOMO)			E(LUMO)			E_g			ERED^2		
	1–1	1–2	2–2	1–1	1–2	2–2	1–1	1–2	2–2	1–1	1–2	2–2
B–H	−7.44	−6.77	−6.54	**−2.91**	**−2.74**	**−2.59**	4.53	3.92	3.94	0.500	0.394	0.237
N–H	−6.15	−5.88	−5.71	**−1.77**	**−2.11**	**−2.30**	4.38	3.77	3.41	0.112	0.113	0.144

Figure S5. HOMO and LUMO distribution of the model compounds corresponding to the moieties of linearly fused aromatic rings including boron and carbonyl group in BCO acceptors

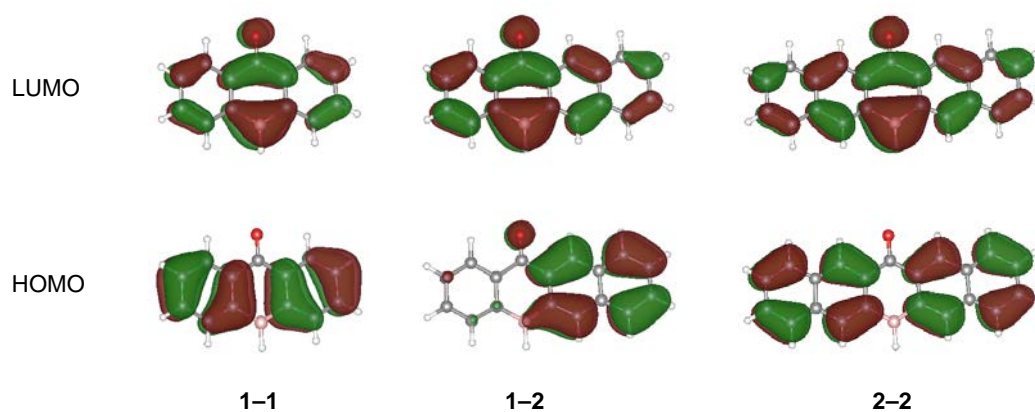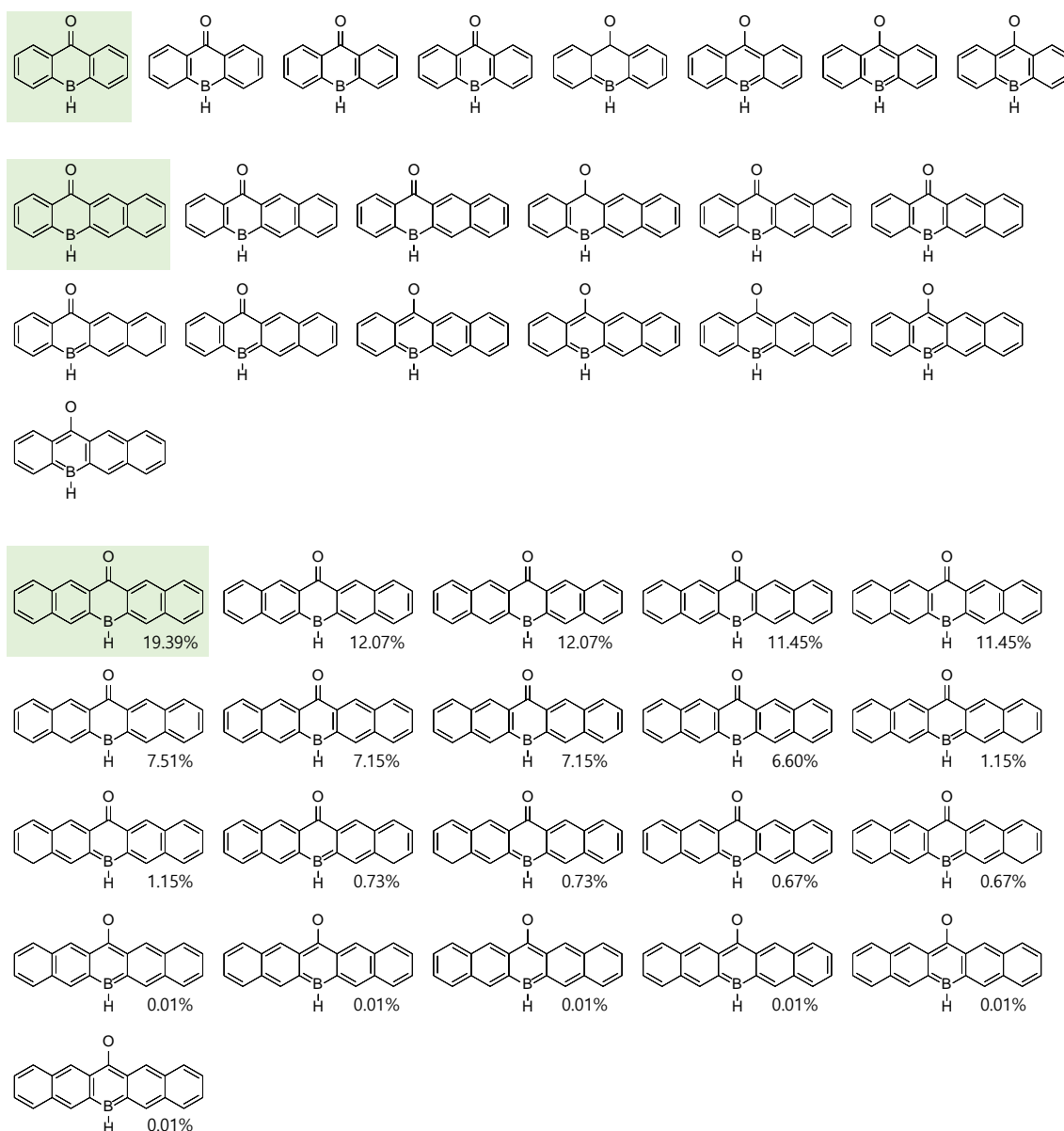**Figure S6.** All Kekulé structures of model compounds corresponding to the moieties of linearly fused aromatic rings including boron and carbonyl group in BCO acceptors, which are arranged in the order of WFRT weight (%). The Kekulé structures as the most dominant resonance contributor are highlighted in green.

| | Hole | Particle | Hole | Particle |

PXZBAO (1)

T_2 (2.63 eV, $^3n\pi^*$) T_4 (2.79 eV, $^3\pi\pi^*$)

PXZBTO (2)

T_2 (2.40 eV, $^3\pi\pi^*$) T_4 (2.73 eV, $^3n\pi^*$)

PXZBPO (3)

T_2 (2.34 eV, $^3\pi\pi^*$) T_8 (2.81 eV, $^3n\pi^*$)
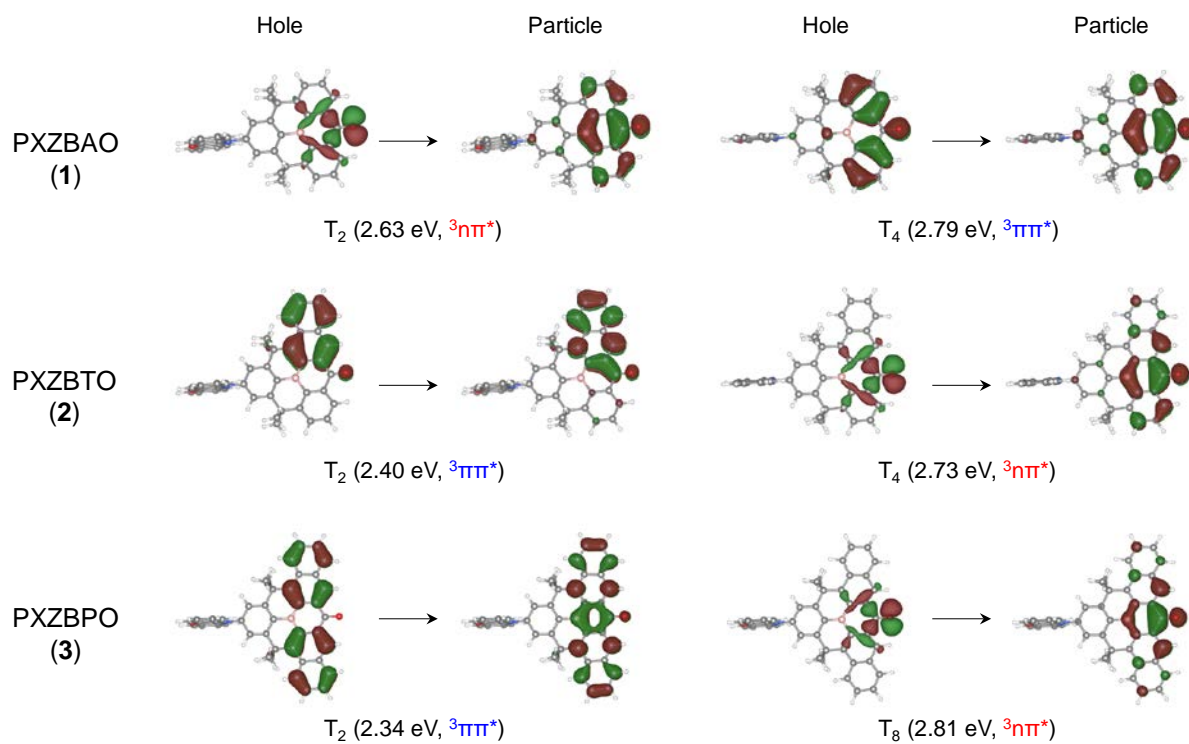
Figure S7. Natural transition orbitals (NTOs) of compounds, **PXZBAO** (**1**), **PXZBTO** (**2**), and **PXZBPO** (**3**), for their lowest-lying $^3n\pi^*$ and $^3\pi\pi^*$ locally excited triplet states at the acceptor moiety (LE$_A$). The excitation energies given in parentheses correspond to the absorption energies from their S$_0$ state.

Figure S8. Natural transition orbitals (NTOs) of donor (PXZH) and acceptors (HBAO, HBTO, HBPO) for the transitions from S_0 to S_1 and/or T_1 states obtained using the TDDFT calculations at the PBE0/6-31G(d,p) level of theory. The adiabatic excitation energies are given in parentheses.

6. Reference

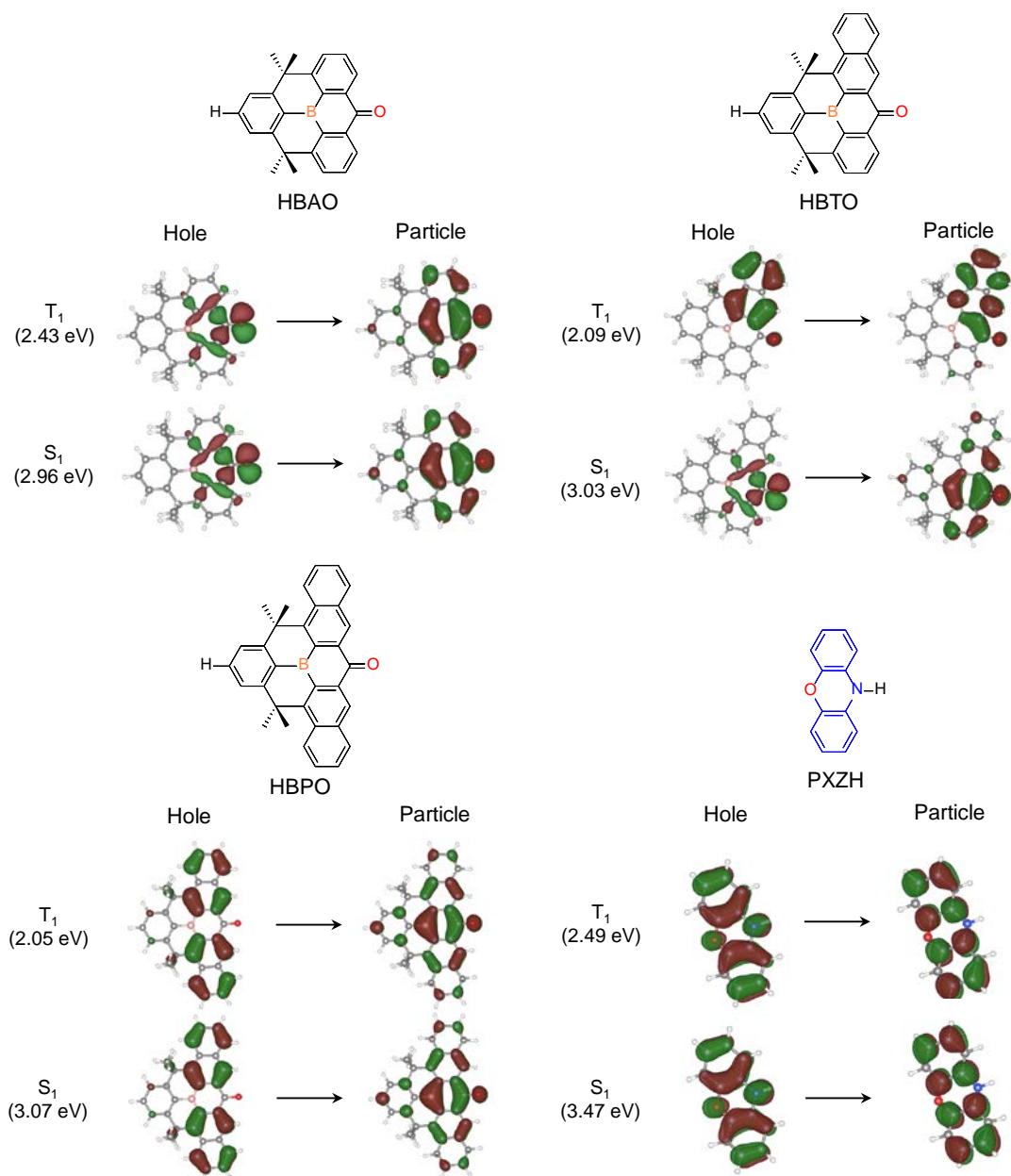1 M. Y. Wong, E. Zysman-Colman, *Adv. Mater.*, **2017**, 29, 1605444.

2 H. Kaji, H. Suzuki, T. Fukushima, K. Shizu, K. Suzuki, S. Kubo, T. Komino, H. Oiwa, F. Suzuki, A. Wakamiya, Y. Murata, C. Adachi, *Nat. Commun.*, **2015**, 6, 8476.

3 Y. Tao, K. Yuan, T. Chen, P. Xu, H. Li, R. Chen, C. Zheng, L. Zhang, W. Huang, *Adv. Mater.*, **2014**, 26, 7931-7958.

4 Q. Zhang, B. Li, S. Huang, H. Nomura, H. Tanaka, C. Adachi, *Nat. Photonics*, **2014**, 8, 326-332.

5 V. Jankus, P. Data, D. Graves, C. McGuinness, J. Santos, M. R. Bryce, F. B. Dias, A. P. Monkman, *Adv. Funct. Mater.,* **2014**, 24, 6178-6186.

6 J. W. Sun, J.-H. Lee, C.-K. Moon, K.-H. Kim, H. Shin, J.-J. Kim, *Adv. Mater.*, **2014**, 26, 5684-5688.

7 F. B. Dias, K. N. Bourdakos, V. Jankus, K. C. Moss, K. T. Kamtekar, V. Bhalla, J. Santos, M. R. Bryce, A. P. Monkman, *Adv. Mater.*, **2013**, 25, 3707-3714.

8 H. Uoyama, K. Goushi, K. Shizu, H. Nomura, C. Adachi, *Nature,* **2012**, 492, 234-238.

9 Y. H. Lee, W. Lee, T. Lee, J. Jung, S.Yoo, and M. H. Lee, *Chem. Eng.J.*, **2023** 452,139387

10 T. Hatakeyama, K. Shiren, K. Nakajima, S. Nomura, S. Nakatsuka, K. Knoshita J. Ni, Y.Ono, T. Ikuta *Adv Mater.* **2016**, 28, 2777-2781.

11 Y. H. Lee, W. Lee, T. Lee, J. Jungm S.Yoo and M. H. Lee Chem. Eng.J. 2021 423, 130224

12 Y. Wang, *J. Chem. Inf. Model.* **2022**, *62*, 5136-5148.

13 S. K. Lower, M. A. El-Sayed, *Chem. Rev.* **1966**, *66*, 199-241

14 Martin, R. M., **2004,** *Electronic Structure: Basic Theory and Practical Methods*, Cambridge University Press.

15 Jensen, F., **1999**, *Introduction to computational chemistry*, Wiley.

16 Szabo, A. & Ostlund, N. S., **1996**, *Modern Quantum Chemistry: Introduction to Advanced Electronic Structure Theory*, Dover Publications.

17 Kohn, W. & Sham, L. J., **1965** *Physical Review* **140**.

18 Parr, R. G. & Yang, W, **1989,** *Density-functional theory of atoms and molecules*, Oxford University Press.

19 Hohenberg, P. & Kohn, W. Inhomogeneous electron gas. Physical Review 136, (1964).

20 Becke, A. D., *Phys Rev A*, **1988**, 38, 3098-3100.

21 Perdew, J. P. & Wang, Y, *Phys Rev B*, **1992**, 45, 13244-13249.

22 Perdew, J. P. et al., *Phys Rev B* **1992** 46, 6671-6687.

23 Perdew, J. P., Burke, K. & Ernzerhof, M., *Phys Rev Lett* **1996**, 77, 3865-3868.

24 E. Runge and E. K. U. Gross 1984 Phys. Rev. Lett. 52, 997

25 Q. Peng, Y. Niu, Q. Shi, X. Gao, Z. Shuai J C. T. C. 2013 9(2) 1132-43

26 R. Núñez, M. Tarrés, A. Ferrer-Ugalde, F. F. de Biani, F. Teixidor, *Chem. Rev.* **2016**, *116*, 14307-14378.

27 R. Núñez, I. Romero, F. Teixidor, C. Viñas, *Chem. Soc. Rev.* **2016**, *45*, 5147-5173.

28 S. Mukherjee, P. Thilagar, *Chem. Commun.* **2016**, *52*, 1070-1093.

29 N. S. Hosmane, *Boron Science: New Technologies and Applications*, CRC Press, New York, **2012**.

30 R. N. Grimes, *Carboranes*, 2nd ed., Academic Press, London, **2011**.

31 D. Tu, P. Leong, S. Guo, H. Yan, C. Lu, Q. Zhao, *Angew. Chem. Int. Ed.* **2017**, *56*, 11370-11374.

32 H. Naito, K. Nishino, Y. Morisaki, K. Tanaka, Y. Chujo, *Angew. Chem. Int. Ed.* **2017**, *56*, 254-259.

33 R. Furue, T. Nishimoto, I. S. Park, J. Lee, T. Yasuda, *Angew. Chem. Int. Ed.* **2016**, *55*, 7171-7175.

34 H. J. Bae, H. Kim, K. M. Lee, T. Kim, Y. S. Lee, Y. Do, M. H. Lee, *Dalton Trans.* **2014**, *43*, 4978-4985

35 N. V. Nghia, S. Park, Y. An, J. Lee, J. Jung, S. Yoo, M. H. Lee, *J. Mater. Chem. C* **2017**, *5*, 3024-3034.

36 Y. Kim, S. Park, Y. H. Lee, J. Jung, S. Yoo, M. H. Lee, *Inorg. Chem.* **2016**, *55*, 909-917.

37 J. Park, Y. H. Lee, J. Y. Ryu, J. Lee, M. H. Lee, *Dalton Trans.* **2016**, *45*, 5667-5675.

38 X. Li, H. Yan, Q. Zhao, *Chem. Eur. J.* **2016**, *22*, 1888-1898.

39 T. Kim, J. Lee, S. U. Lee, M. H. Lee, *Organometallics* **2015**, *34*, 3455-3458.

40 Y. H. Lee, J. Park, J. Lee, S. U. Lee, M. H. Lee, *J. Am. Chem. Soc.* **2015**, *137*, 8018-8021.

41 Y. H. Lee, J. Park, S.-J. Jo, M. Kim, J. Lee, S. U. Lee, M. H. Lee, *Chem. Eur. J.* **2015**, *21*, 2052-2061.

42 H. J. Bae, J. Chung, H. Kim, J. Park, K. M. Lee, T.-W. Koh, Y. S. Lee, S. Yoo, Y. Do, M. H. Lee, *Inorg. Chem.* **2014**, *53*, 128-138.

43 H. J. Bae, H. Kim, K. M. Lee, T. Kim, M. Eo, Y. S. Lee, Y. Do, M. H. Lee, *Dalton Trans.* **2013**, *42*, 8549-8552.

44 T. Kim, H. Kim, K. M. Lee, Y. S. Lee, M. H. Lee, *Inorg. Chem.* **2013**, *52*, 160-168.

45 R. N. Grimes, *Dalton Trans.* **2015**, *44*, 5939-5956.

46 A. M. Spokoyny, *Pure Appl. Chem.* **2013**, *85*, 903-919.

47 Z. Chen, R. B. King, *Chem. Rev.* **2005**, *105*, 3613-3642.

48 R. B. King, *Chem. Rev.* **2001**, *101*, 1119-1152.

49 V. I. Bregadze, *Chem. Rev.* **1992**, *92*, 209-223.

50 R. E. Williams, *Chem. Rev.* **1992**, *92*, 177-207.

51 A. Ferrer-Ugalde, A. González-Campo, C. Viñas, J. Rodríguez-Romero, R. Santillan, N. Farfán, R. Sillanpää, A. Sousa-Pedrares, R. Núñez, F. Teixidor, *Chem. Eur. J.* **2014**, *20*, 9940-9951.

52 C. Shi, H. Sun, X. Tang, W. Lv, H. Yan, Q. Zhao, J. Wang, W. Huang, *Angew. Chem. Int. Ed.* **2013**, *52*, 13434-13438.

53 A. Ferrer-Ugalde, E. J. Juárez-Pérez, F. Teixidor, C. Viñas, R. Sillanpää, E. Pérez-Inestrosa, R. Núñez, *Chem. Eur. J.* **2012**, *18*, 544-553.

54 J. M. Oliva, N. L. Allan, P. v. R. Schleyer, C. Viñas, F. Teixidor, *J. Am. Chem. Soc.* **2005**, *127*, 13538-13547.

55 Ivan V. Glukhov, Mikhail Y. Antipin, Konstantin A. Lyssenko, *Eur. J. Inorg. Chem.* **2004**, *2004*, 1379-1384.

56 L. A. Boyd, W. Clegg, R. C. B. Copley, M. G. Davidson, M. A. Fox, T. G. Hibbert, J. A. K. Howard, A. Mackinnon, R. J. Peace, K. Wade, *Dalton Trans.* **2004**, 2786-2799.

57 J. Llop, C. Viñas, J. M. Oliva, F. Teixidor, M. A. Flores, R. Kivekas, R. Sillanpää, *J. Organomet. Chem.* **2002**, *657*, 232-238.

58 J. Llop, C. Viñas, F. Teixidor, L. Victori, R. Kivekäs, R. Sillanpää, *Organometallics* **2001**, *20*, 4024-4030.

59 Y. Morisaki, M. Tominaga, T. Ochiai, Y. Chujo, *Chem. Asian J.* **2014**, *9*, 1247-1251.

60 L. Weber, J. Kahlert, R. Brockhinke, L. Böhling, J. Halama, A. Brockhinke, H.-G. Stammler, B. Neumann, C. Nervi, R. A. Harder, M. A. Fox, *Dalton Trans.* **2013**, *42*, 10982-10996.

61 L. Weber, J. Kahlert, L. Böhling, A. Brockhinke, H.-G. Stammler, B. Neumann, R. A. Harder, P. J. Low, M. A. Fox, *Dalton Trans.* **2013**, *42*, 2266-2281.

62 Y. Morisaki, M. Tominaga, Y. Chujo, *Chem. Eur. J.* **2012**, *18*, 11251-11257.

63 L. Weber, J. Kahlert, R. Brockhinke, L. Böhling, A. Brockhinke, H.-G. Stammler, B. Neumann, R. A. Harder, M. A. Fox, *Chem. Eur. J.* **2012**, *18*, 8347-8357.

64 T. Matulaitis, P. Imbrasas, N. A. Kukhta, P. Baronas, T. Bučiūnas, D. Banevičius, K. Kazlauskas, J. V. Gražulevičius, S. Juršėnas, *J. Phys. Chem. C* **2017**, *121*, 23618-23625.

65 Y. H. Lee, S. Park, J. Oh, J. W. Shin, J. Jung, S. Yoo, M. H. Lee, *ACS Appl. Mater. Interfaces* **2017**, *9*, 24035-24042.

66 N. V. Nghia, J. Oh, J. Jung, M. H. Lee, *Organometallics* **2017**, *36*, 2573-2580.

67 S. W. Kwak, B. H. Choi, J. H. Lee, H. Hwang, J. Lee, H. Kwon, Y. Chung, K. M. Lee, M. H. Park, *Inorg. Chem.* **2017**, *56*, 6039-6043.

68 K. C. Song, H. Kim, K. M. Lee, Y. S. Lee, Y. Do, M. H. Lee, *Dalton Trans.* **2013**, *42*, 2351-2354.

69 Y. Geng, A. D'Aleo, K. Inada, L.-S. Cui, J. U. Kim, H. Nakanotani, C. Adachi, *Angew. Chem. Int. Ed.* **2017**, *56*, 16536-16540.

70 H. Uoyama, K. Goushi, K. Shizu, H. Nomura, C. Adachi, *Nature* **2012**, *492*, 234-238.

71 Y. Zhao, D. G. Truhlar, *J. Phys. Chem. A* **2006**, *110*, 13126-13130.

72 Y. Tao, K. Yuan, T. Chen, P. Xu, H. Li, R. Chen, C. Zheng, L. Zhang, W. Huang, *Adv. Mater.* **2014**, *26*, 7931-7958.

73 A. Endo, M. Ogasawara, A. Takahashi, D. Yokoyama, Y. Kato, C. Adachi, *Adv. Mater.* **2009**, *21*, 4802-4806

74 T. Kim, H. Kim, K. M. Lee, Y. S. Lee and M. H. Lee, *Inorg. Chem.*, **2013**, 52, 160.

75 Hirata, S.; Head-Gordon, M. *Chem. Phys. Lett.* **1999**, *314*, 291-299.

76 Adamo, C.; Barone, V. *J. Chem. Phys.* **1999**, *110*, 6158-6169

77. Frisch, M. J.; Trucks, G. W.; Schlegel, H. B.; Scuseria, G. E.; Robb, M. A.; Cheeseman, J. R.; Scalmani, G.; Barone, V.; Petersson, G. A.; Nakatsuji, H.; Li, X.; Caricato, M.; Marenich, A. V.; Bloino, J.; Janesko, B. G.; Gomperts, R.; Mennucci, B.; Hratchian, H. P.; Ortiz, J. V.; Izmaylov, A. F.; Sonnenberg, J. L.; Williams-Young, D.; Ding, F.; Lipparini, F.; Egidi, F.; Goings, J.; Peng, B.; Petrone, A.; Henderson, T.; Ranasinghe, D.; Zakrzewski, V. G.; Gao, J.; Rega, N.; Zheng, G.; Liang, W.; Hada, M.; Ehara, M.; Toyota, K.; Fukuda, R.; Hasegawa, J.; Ishida, M.; Nakajima, T.; Honda, Y.; Kitao, O.; Nakai, H.; Vreven, T.; Throssell, K.; Montgomery, J. A., Jr.; Peralta, J. E.; Ogliaro, F.; Bearpark, M. J.; Heyd, J. J.; Brothers, E. N.; Kudin, K. N.; Staroverov, V. N.; Keith, T. A.; Kobayashi, R.; Normand, J.; Raghavachari, K.; Rendell, A. P.; Burant, J. C.; Iyengar, S. S.; Tomasi, J.; Cossi, M.; Millam, J. M.; Klene, M.; Adamo, C.; Cammi, R.; Ochterski, J. W.; Martin, R. L.; Morokuma, K.; Farkas, O.; Foresman, J. B.; Fox, D. J. Gaussian 16, Revision A.03, Gaussian, Inc., Wallingford CT, **2016**

78. J. Tomasi, B. Mennucci, R. Cammi, *Chem. Rev.* **2005**, *105*, 2999-3094.

79 P. K. Samanta, D. Kim, V. Coropceanu, J.-L. Brédas, *J. Am. Chem. Soc.* **2017**, *139*, 4042-4051.

80 F. B. Dias, J. Santos, D. R. Graves, P. Data, R. S. Nobuyasu, M. A. Fox, A. S. Batsanov, T. Palmeira, M. N. Berberan-Santos, M. R. Bryce, A. P. Monkman, *Adv. Sci.* **2016**, *3*, 1600080.

81 P. Data, P. Pander, M. Okazaki, Y. Takeda, S. Minakata, A. P. Monkman, *Angew. Chem. Int. Ed.* **2016**, *55*, 5739-5744.

82 M. Baba, *J. Phys. Chem. A* **2011**, *115*, 9514-9519

83 M. K. Etherington, J. Gibson, H. F. Higginbotham, T. J. Penfold, A. P. Monkman, *Nat. Commun.* **2016**, *7*, 13680.

84 P. K. Samanta, D. Kim, V. Coropceanu, J.-L. Brédas, *J. Am. Chem. Soc.* **2017**, *139*, 4042-4051.

85 F. B. Dias, J. Santos, D. R. Graves, P. Data, R. S. Nobuyasu, M. A. Fox, A. S. Batsanov, T. Palmeira, M. N. Berberan-Santos, M. R. Bryce, A. P. Monkman, *Adv. Sci.* **2016**, *3*, 1600080.

86 P. Data, P. Pander, M. Okazaki, Y. Takeda, S. Minakata, A. P. Monkman, *Angew. Chem. Int. Ed.* **2016**, *55*, 5739-5744.

87 M. Baba, *J. Phys. Chem. A* **2011**, *115*, 9514-9519.

88 Y. Wada, H. Nakagawa, S. Matsumoto, Y. Wakisaka, H. Kaji, *Nat. Photonics* **2020**, *14*, 643-649.

89 J. U. Kim, I. S. Park, C.-Y. Chan, M. Tanaka, Y. Tsuchiya, H. Nakanotani, C. Adachi, *Nat. Commun.* **2020**, *11*, 1765.

90 H. Noda, X.-K. Chen, H. Nakanotani, T. Hosokai, M. Miyajima, N. Notsuka, Y. Kashima, J.-L. Brédas, C. Adachi, *Nat. Mater.* **2019**, *18*, 1084-1090.

91 I. S. Park, K. Matsuo, N. Aizawa, T. Yasuda, *Adv. Funct. Mater.* **2018**, *28*, 1802031.

92 H. Noda, H. Nakanotani, C. Adachi, *Sci. Adv.* **2018**, *4*, eaao6910.

93 T. J. Penfold, E. Gindensperger, C. Daniel, C. M. Marian, *Chem. Rev.* **2018**, *118*, 6975-7025.

94 J. Gibson, A. P. Monkman, T. J. Penfold, *ChemPhysChem* **2016**, *17*, 2956-2961.

95 N. Aizawa, A. Matsumoto, T. Yasuda, *Sci. Adv.* **2021**, *7*, eabe5769

96 Q. Zhang, H. Kuwabara, W. J. Potscavage, Jr., S. Huang, Y. Hatae, T. Shibata, C. Adachi, *J. Am. Chem. Soc.* **2014**, *136*, 18070-18081.

97 M. Bixon, J. Jortner, J. Cortes, H. Heitele, M. E. Michel-Beyerle, *J. Phys. Chem.* **1994**, *98*, 7289-7299.

98 M. Belletête, G. Durocher, S. Hamel, M. Côté, S. Wakim, M. Leclerc, *J. Chem. Phys.* **2005**, *122*, 104303.

99 P. L. Santos, J. S. Ward, P. Data, A. S. Batsanov, M. R. Bryce, F. B. Dias, A. P. Monkman, *J. Mater. Chem. C* **2016**, 4, 3815-3824.

100 *Dalton, a molecular electronic structure program*, Release v2018.0 (**2018**), see http://daltonprogram.org.

101 T. Lu, F. Chen, *J. Comput. Chem.* **2012**, *33*, 580-592.

102 A. D. Becke. *J. Chem. Phys.* **1993**, *98*, 5648-5652.

103 The EzReson program, https://github.com/yangwangmadrid/EzReson

104 H. J. Kim and T. Yasuda, *Adv.OpticalMater.***2022**, 10, 2201714.

105 Russell N. Grimes, **2011**, *Carboranes*, Acade,om press.

Appendix. Bibliography
List of recently research paper
5. H. Lee, N. T. N. Nguyen, J. Jung, J. -H. Lee, and M. H. Lee, Bulky group decorated multi-resonance TADF emitters, in preparation.
4. H. Sato, T. Lee, M. Lee, E. Kazuma, J. Jung, K. C. Ko, Y. Kim, and T. K. Shimizu, STM and DFT studies for a photochromic molecule adsorbed on Cu(111), in preparation.
3. Young Hoon Lee (§), Jeoungmin Ji (§), Thi Quyen Tran, Taehwan Lee, Jaehoon Jung, Youngil Lee*, Seunghyup Yoo*, and Min Hyung Lee*, TADF emitters based on tri-spiral acridine donor and spiro-B-heterotriangulene acceptor: toward high horizontal dipole orientation and high-efficiency deep-blue OLEDs. submitted (2023)
2. H. Mubarok, A. Amin, T. Lee, H. Jung, J. -H. Lee, and M. H. Lee, Triptycene-fused sterically shielded multi-resonance TADF emitter enables high-efficiency deep blue OLEDs with reduced Dexter energy transfer. Angew. Chem. Int. Ed. in press (2023)
1. I. N. Istiqomah (§), J. H. Jang (§), T. Lee (§), Y. H. Lee, C. Kim, J. Jung, J.-H. Lee, and M. H. Lee, Impact of π-expanded boron-carbonyl hybrid acceptors on TADF properties: controlling local triplet excited states and unusual emission tuning. *ACS Appl. Mater. Interfaces 15*, 15758-15767 (2023).

List of D-A typr TADF paper
9. K. Shin, E. Lee, T. Lee, Y. H. Lee, D. H. Kim, C. Kim, J. Jung, B. J. Jung, and M. H. Lee *Dyes Pigments* 209, 110937 (2023).
8. Y. H. Lee, W. Lee, T. Lee, J. Jung, S. Yoo, and M. H. Lee *Chem. Eng. J.* 452, 139387 (2023).
7. Y. H. Lee, Y.-S. Shin, T. Lee, J. Jung, J.-H. Lee, and M. H. Lee, *Chem. Eng. J.* 423, 130224 (2021).
6. Y. H. Lee, W. Lee, T. Lee, D. Lee, J. Jung, S. Yoo, and M. H. Lee, *ACS Appl. Mater. Interfaces*, 13, 45778-45788 (2021).
5. Y. H. Lee, D. Lee, T. Lee, J. Lee, J. Jung, S. Yoo, and M. H. Lee, *Dyes Pigments* 118, 109224 (2021).
4. A. Kumar, H. Y. Shin, T. Lee, J. Jung, B. J. Jung, and M. H. Lee, *Chem. Eur. J.* 26, 16793-16801 (2020).
3. H. Mubarok, W. Lee, T. Lee, J. Jung, S. Yoo, and M. H. Lee, *Front. Chem.* 8, 538 (2020).
2. J. Kim, T. Lee, J. Y. Ryu, Y. H. Lee, J. Lee, J. Jung, and M. H. Lee, *Organometallics* 39, 2235-2244 (2020).
1. A. Kumar, W. Lee, T. Lee, J. Jung, S. Yoo, and M. H. Lee, *J. Mater. Chem. C* 8, 4253-4263 (2020)

List of normal fluorescence paper
2. N. T. N. Nguyen, H. Mubarok, T. Lee, T. Q. Tran, J. Jung, and M. H. Lee, *RSC Adv*. 12, 29892-29899 (2022).
1. I. N. Istiqomah, H. Mubarok, T. Lee, N. T. N. Nguyen, J. Jung, and M. H. Lee, *Bull. Korean Chem. Soc*. 43(2), 293-298 (2022).

Thank you for Prof. Jung, Prof. Lee, CMSL members and FMFM members.